Università Degli Studi di Padova

Dipartimento di Fisica e Astronomia "Galileo Galilei"

Master Degree in Physics

of the fundamental interactions

Sachdev-Ye-Kitaev quantum batteries

Relatore
Prof. Luca Dell'Anna

Laureando
Giovanni Sisorio

Academic Year 2023/2024

Abstract

Quantum batteries utilize quantum effects to achieve more efficient and rapid charging processes compared to classical systems. Dynamics driven by quantum quenches in the SYK model and its generalizations are the main subject of the work. Specifically the quenches find applications in charging quantum batteries. A quantum battery is a quantum device useful to store and release energy coherently, namely it is a quantum mechanical system designed for energy storage. Generally it can be composed by several quantum cells, namely n-level quantum systems, which can be excited by switching on and off an additional "charger" Hamiltonian during the time interval of the cycle. A possibility is to employ the SYK model as charger quench Hamiltonian. The student will study, therefore, the effects of quantum quenches involving the SYK model for different choices of the coupling. The charging time, the associated power and the amount of extractable work, can then be analyzed.

Acknowledgements

I want to thank professor Luca Dell'Anna for helping me focus on the important aspects of the thesis, and for introducing me to this innovative topic. Furthermore, thanks go to my friends and the people I have met over the years and who have made every day interesting. And of course a heartfelt thanks to my family who has supported me over the past few years.

Contents

List of Figures

Chapter 1

Introduction

Quantum technologies have garnered significant attention in recent years due to their potential to revolutionize fields such as computation, communication, and energy storage. Among these innovations, quantum batteries stand out as a novel application, leveraging the principles of quantum mechanics to surpass classical limits in energy storage and charging processes. Unlike conventional batteries, where energy is stored and transferred through classical processes, quantum batteries utilize quantum coherence and entanglement, offering the possibility of faster and more efficient energy dynamics. There are examples of real systems that can be used as quantum batteries, for instance chains of interacting spins, quantum dots, superconducting qubits, ions trapped in electromagnetic fields and cavity QED systems

At the heart of these systems lies the concept of quantum quenches, which involve sudden changes in the Hamiltonian of a quantum system, leading to dynamic evolutions that can be harnessed to drive charging processes. This is particularly intriguing in the context of complex quantum models such as the Sachdev-Ye-Kitaev (SYK) model.

It was initially developed by Subir Sachdev and Jinwu Ye in the early 1990s and later refined by Alexei Kitaev around 2015. It describes a system of N Majorana fermions and it was developed to explore connections between condensed matter physics and black hole thermodynamics. The SYK model has emerged as a powerful framework to study strongly correlated fermionic systems with chaotic dynamics and the model's rich structure, characterized by random all-to-all interactions between fermions, offers an ideal playground for understanding non-equilibrium quantum dynamics.

In this work, we explore the application of the SYK model in quantum battery systems. Specifically, we study the role of quantum quenches in the SYK model as a mechanism for driving the charging of quantum batteries. A quantum battery can be conceptualized as a quantum system composed of multiple quantum cells, where the energy storage and extraction processes are governed by coherent quantum effects. By applying an SYK-type Hamiltonian as a quench charger, we aim to investigate the influence of different couplings on key metrics such as charging time, power output, and the extractable work.

This approach not only provides a pathway to optimize the performance of quantum batteries but also offers deeper insights into the interplay between quantum chaos, many-body physics, and energy transfer in quantum systems.

1.1 Thesis description

Chapter 2: Quantum Batteries This chapter introduces the concept of quantum batteries, setting a general context and outlining various approaches to their charging mechanisms. Section 2.1 presents the general context of quantum batteries, focusing on their theoretical foundations and practical motivations. Subsections delve into specific approaches, beginning with the charging approach in Section 2.1.1, and extending to the passive state and the concept of ergotropy, that represents the extractable work in a quantum system, in Section 2.2. Section 2.3 examines the power and quantum advantage, discussing parameters such as charging power, quantum speed limit time, and quantum advantage, which highlight the benefits of quantum over classical systems in energy storage and retrieval. Finally, Section 2.4 connects these concepts to the quantum speed limit and quantum charging distance, providing useful theoretical bound used to test the constructed models.

Chapter 3: SYK Model Chapter 3 provides a comprehensive overview of the SYK model, a prominent theoretical framework in quantum chaos and quantum information. Section 3.1 offers a review of the model, with a focus on its connection to chaos (3.1.1) and thermalization (3.1.2). Sections 3.2 and 3.3 introduce the two-point and four-point functions, respectively, which are essential for studying quantum correlations within the SYK framework. A discussion on entropy is included in Section 3.2.1. Sections 3.4 and 3.5 extend the analysis to the sparse and complex SYK models, exploring modified versions of the model that are relevant for understanding sparsity and complexity in quantum systems. The chapter concludes with Section 3.6, which discusses the relation between quantum chaos and sparsity, including quantitative tools such as the spectral form factor and nearest-neighbor gap ratio, as well as defining transition points within the system.

Chapter 4: SYK quantum batteries analysis This chapter addresses the practical calculations involved in SYK quantum batteries. Section 4.1 introduces SYK quantum batteries, focusing on charging protocols and population dynamics in Sections 4.1.1 and 4.2. Sections 4.3 and 4.4 cover critical bounds on charging power and quantum charging distance, which define the limits of performance and temporal efficiency in these systems. Section 4.5 presents a detailed discussion on time evolution and ergotropy, examining the evolution of stored energy in SYK batteries. Section 4.6 focuses on charging stability, addressing aspects like charging ratio (4.6.1), fluctuations (4.6.2), and efficiency (4.6.3). In the final sections of the chapter, 4.7 and 4.8, we introduce the concept of sparse SYK quantum batteries, examining how sparsity influences the charging ratio, efficiency, and fluctuations; then we consider the case of the disorder-free QB and the most important features of these type of batteies.

A.1 More on the Liouville-von Neumann equation In this section we analyze in more detail the Liouville-von Neumann equation. In particular we clarify the relation between the equation and the unitary evolution of the density matrix.

A.2 More on Chaos This section elaborates on the concept of chaos, particularly within the context of quantum systems. It provides additional theoretical background on quantum chaos, extending the discussion from Chapter 3.

A.3 More on Sparsification This section delves into expander graphs. Expander graphs are a type of sparse graph with strong connectivity properties, making them highly relevant for modeling efficient, sparse interactions in quantum systems.

A.4 More on Random Matrix Theory This section offers a deeper dive into Random Matrix Theory (RMT), which is critical to understanding the statistical behavior of eigenvalues in complex quantum systems, such as those modeled by the SYK Hamiltonian.

A.5 Hopping Operator Section A.5 discusses the thermalization property for a non extensive operator as the Hopping operator

Chapter 2

Quantum Batteries

Quantum batteries represent a promising paradigm for the storage and transfer of energy at the quantum level, offering significant advantages over their classical counterparts. In this chapter, we explore the fundamental aspects of quantum batteries, beginning with their structure and the charging approach introduced by Alicki and Fannes in 2013 [3], which laid the foundation for the field. This framework emphasizes how quantum systems can be charged and discharged, using specific Hamiltonians that drive the energy storage process.

We then delve into the concept of passive states and the notion of ergotropy, as developed by llahverdyan, Balian, and Nieuwenhuizen in 2004 [4]. These ideas are crucial for understanding the limits of extractable work from quantum systems and how energy can be optimally harnessed in a quantum battery.

A key advantage of quantum batteries lies in the potential for quantum enhancement or quantum advantage, which allows for faster charging times and higher efficiency compared to classical systems. This concept has been thoroughly examined by Binder and Campaioli [5], who demonstrated how quantum coherence and entanglement can speed up the charging process, providing a distinct quantum advantage.

Finally, we address the idea of quantum charging distance, as introduced by Gyhm [14], which quantifies the distance a system must traverse in Hilbert space to achieve full charging. This concept provides a geometric perspective on the charging process, offering insights into how efficiently a quantum battery can be charged.

Throughout this chapter, we follow the approach presented by Campaioli, Gherardini, Quach, Polini, and Andolina [6] due to the clarity and thoroughness of their exposition.

2.1 General context

A quantum battery is defined as a d-dimensional system governed by an internal Hamiltonian H_0. This Hamiltonian is characterized by a spectrum of non-degenerate energy levels presented as [3]:

$$H_0 = \sum_{k=1}^{d} \epsilon_k |k\rangle\langle k|, \quad \epsilon_{k+1} > \epsilon_k. \tag{2.1}$$

It is important to note that many authors, such as Campaioli[6] use a less stringent condition considering $\epsilon_{k+1} \geq \epsilon_k$. This can be assumed as long as the difference between the biggest $\epsilon_{\max}$ and the smallest eigenvalues $\epsilon_{\min}$ is bigger than zero; this condition is equivalent to required that the QB Hamiltonian H_0 has a bandwidth grater than zero:

$$\omega(H_0) \equiv \epsilon_{\max} - \epsilon_{\min} > 0. \tag{2.2}$$

The quantum state of the QB at general time t can be described with a density matrix $\rho(t)$ and the energy associated to it can be written as $\langle H_0\rangle_\rho = Tr[H_0\rho(t)]$. We will indicate with $\rho_0 = \rho(0)$ the initial state of the battery and the time evolution of ρ_0 to $\rho(t)$ is obtain with the Liouville-von Neumann equation

$$\frac{d}{dt}\rho(t) = -i[H_0 + H_1(t), \rho(t)] \tag{2.3}$$

where $H_1(t)$ is a time-dependent interacting Hamiltonian. In the context of QBs the $H_1(t)$ is often called "charging Hamiltonian" since it is used to inject energy in the battery.

The Liouville-von Neumann equation describes the time evolution of the density matrix in a closed quantum system. This equation ensures the unitary evolution of the quantum state preserving both the trace and the hermiticity of $\rho(t)$ over time. In the context of quantum batteries, this formalism is crucial as it governs how energy is exchanged, coherence is maintained, and charging processes are analyzed.

From eqaution 2.3 naturally follows the concept of stored energy at time t expressed as [3]:

$$W(t) = Tr[H_0\rho(t)] - Tr[H_0\rho_0] \tag{2.4}$$

As we will see better leter in the work, the charging Hamiltonian is often applied to the system at time $t = 0$ and turned off at time $t = \tau$; the state at time τ can be relate to the initial state by the transformation:

$$\rho(\tau) = U(\tau)\rho_0 U^\dagger(\tau) \tag{2.5}$$

that is unitary and where the operator $U(\tau)$ is given by:

$$U(\tau) = T\exp(-i\int_0^\tau ds[H_0 + H_1(s)]) \tag{2.6}$$

where T is the time ordering operator.

Since we are dealing with unitary transformation, the extraction and storing of energy in the QB are opposite procedures and we can write:

$$W(t)_{\text{extracted}} = \text{Tr}[H_0\rho_0] - \text{Tr}[H_0\rho(t)]. \tag{2.7}$$

We now show a different definition for the QB, used by Alicki and Fannes (2013)[3] which will be useful later in the work. The Hamiltonian take the form:

$$H_0^{(N)} = \sum_{i=1}^{N} H_i \tag{2.8}$$

where $H_0^{(N)}$ is the total quantum battety Hamiltonian (defined before as H_0) and and H_i represents the i-th constituent of the total Hamiltonian. This was introduce to describe composite quantum systems made up of multiple independent parts; in particular it is useful for the study of entangling batteries.

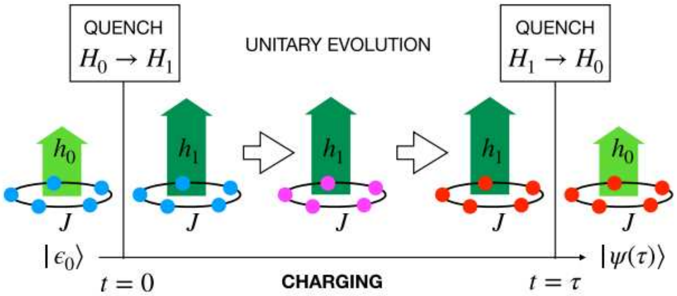

Figure 2.1: Quantum battery charging process depicted through quench dynamics. Initially, the battery starts in the ground state $|\epsilon_0\rangle$ under Hamiltonian H_0 at $t = 0$. A sudden quench switches the system to Hamiltonian H_1, initiating unitary evolution that charges the battery. At $t = \tau$, a second quench reverts the Hamiltonian back to H_0, stabilizing the battery in the charged state $|\psi(\tau)\rangle$. This sequence illustrates the interplay between energy states and Hamiltonian transitions in the charging mechanism. From [9]

.

2.1.1 Charging approach

The methodologies for storing energy within quantum batteries can fundamentally be classified into two distinct paradigms: *parallel* (local) charging and *collective* (global) charging. These strategies differ primarily in their interaction schemas as described by the Hamiltonian in Equation 2.8.

In the parallel charging approach, energy is stored by independently charging each of the N subsystems comprising the quantum battery. This method uses a localized Hamiltonian for each subsystem, facilitating isolated control and energy transfer. The energy stored using this approach, typically denoted in the literature as $W_{\parallel}$, allows for simplicity in manipulation but may not exploit potential quantum correlations between subsystems.

Conversely, the collective charging approach exploits the intrinsic quantum properties such as entanglement and superposition by applying an interacting Hamiltonian that encompasses multiple, if not all, subsystems simultaneously. This method, indicated by $W_{\sharp}$, aims to optimize the charging process through global operations. By engaging multiple subsystems, collective charging can potentially enhance the energy storage capacity and charging speed of the quantum battery, tapping into the cooperative effects that arise from quantum mechanics.

Each charging strategy has its merits and ideal applications, influenced by factors like the intended use, scalability of the system, and technological limitations. The choice between parallel and collective charging depends on the trade-off between operational complexity and the efficiency gains from exploiting quantum mechanical effects.

2.2 The passive state and the ergotropy

The important concept of *ergotropy* was introduced by Allahverdyan, Balian and Nieuwenhuizen in 2004[4] and it represents the maximal amount of work that can be extracted from a state ρ via unitary operation; in other words it quantifies the available energy in a battery[5]. In this work we will refer to that with $\mathcal{E}$.

2.2.1 Passive and completely passive state

In order to discuss about the ergotropy it is important to define another important object: the *passive state*. We refer to it as a state from which no further work can be extracted by means of cyclic processes. For cyclic processes we refer to a process in which the potential (in this context the charging Hamiltonian) is zero before $t = 0$ and for $t > \tau$ that is $H_1(0) = H_1(\tau) = 0$. More intuitively when a system is passive, it is in thermodynamic equilibrium and the energy levels are already "optimally" populated. Moreover, we saw that the energy associated to a sate is $\mathrm{Tr}[H_0\rho]$ and the maximum value of it is reached when the state is a thermal state (i.e. in thermal equilibrium with a bath):

$$\rho(\tau) = \frac{e^{-\beta H_0}}{Z}, \tag{2.9}$$

where β is the inverse of the temperature and Z is the partition function. Since all thermal states commute with the Hamiltonian H_0 they are passive.

Before continuing with ergotropy we can show other important result from Alicki and Fannes [3]. Let us consider the QB composed of N constituents described in the Hamiltonian 2.8 and a general state σ; σ is called *completely passive* if the union of N copies of this state remains passive, i.e. if $\otimes^N \sigma = \otimes_{j=1}^N \sigma$ is passive. Furthermore Alicki and Fannes arrived to the conclusion that a state is completely passive if and only if it is a Gibbs state i.e. a thermal state.

2.2.2 Computation of the ergotropy

Returning to ergotropy, it can be expressed as [4]:

$$\mathcal{E}(\rho) \equiv \mathrm{Tr}[H_0\rho] - \min_{U\in SU(d)} \left\{\mathrm{Tr}[H_0 U\rho U^\dagger]\right\}, \tag{2.10}$$

where the optimization is done with respect to unitary operators U in the special unitary group $SU(d)$. The passive state is precisely that for which $\mathrm{Tr}[H_0\rho] \leq \mathrm{Tr}[H_0 U\rho U^\dagger]$ and it turns out that there are two condition that characterize such a state: it commutes with H_0 (i.e. it is diagonal in the basis of H_0)

and its eigenvalues are ordered in a non-increasing way. Therefore we can write the ergotropy in terms of the passive state:

$$\mathcal{E}(\rho) = \mathrm{Tr}[H_0\rho] - \mathrm{Tr}[H_0\sigma_\rho]. \tag{2.11}$$

We can try to construct the ergotropy in a more formal way, following the initial definition by Allahverdyan[4]. We start considering the spectral decomposition of ρ_0 and H_0:

$$\rho_0 = \sum_{k\geq 1} r_k |r_k\rangle\langle r_k|, \quad H = \sum_{j\geq 1} \epsilon_j |\epsilon_j\rangle\langle\epsilon_j|. \tag{2.12}$$

Now we can exploit the fact that for any state ρ there exists a unique passive state denote as σ_ρ; this is obtained via a unitary operation such that:

$$\rho_0 = \sum_{k\geq 1} r_k |r_k\rangle\langle r_k| \quad \longrightarrow \quad \sigma_\rho(0) = U\rho_0 U^\dagger = \sum_{k\geq 1} r_k^{'} |r_k\rangle\langle r_k|, \tag{2.13}$$

where $\{r_k^{'}\}$ represents the same eigenvalues as $\{r_k\}$ sorted in non-increasing order. The state at time $t = \tau$ can be decomposed as:

$$\sigma_\rho(\tau) = \sum_j r_k^{'} |\epsilon_k\rangle\langle\epsilon_k|. \tag{2.14}$$

From this definition the equation 2.10 can be written as:

$$\mathcal{E}(\rho) = \sum_{k,j} r_k \epsilon_j \left(|\langle r_k|\epsilon_j\rangle|^2 - \delta_{kj} \right). \tag{2.15}$$

It is important to highlight the relation between ergotropy and work; the stored energy in eq.2.4 represents the total energy stored in the battery at time t and it includes both extractable and non extractable energy. Therefore the ergotropy (the extractable energy) is only a part of the total energy and this implies:

$$W(t) \geq \mathcal{E}(t) \quad \text{for any time t.} \tag{2.16}$$

The two quantities are equal when the system is highly active, in other words when the energy associated to the passive states is zero. An exemple of this situation is when the system presents maximally coherent states.

Alicki and Fannes [3] found an upper bound for the ergotropy starting from the concept of completely passive state discussed before. Starting from the usual N-components battery they constructed the ergotropy per copy $\mathcal{E}(N)$:

$$\varepsilon(N) \equiv \frac{1}{N} \left(\mathrm{Tr}[H_0^{(N)} \otimes^N \rho] - \mathrm{Tr}[H_0^{(N)} \sigma_{\otimes^N} \rho] \right). \tag{2.17}$$

If we consider $N \to \infty$ the ergotropy for copy is reduced to a more workable expression:

$$\mathcal{E}(\rho) \leq \mathrm{Tr}[H_0\rho(t)] - \mathrm{Tr}[H_0\omega_{\overline{\beta}}], \tag{2.18}$$

where ρ and $\omega_{\overline{\beta}}$ have the same von Neumann entropy $S(\rho) = S(\omega_{\overline{\beta}})$.

2.3 Power and quantum advantage

The idea behind the concept of a quantum battery is obviously to gain some kind of advantage with respect to a classical battery. The first to study this problem were Binder *er al.* in 2015[5] followed by Campaioli *et al.* [7] and others. We start by analyzing the power and than focusing on the concept of quantum advantage.

2.3.1 Charging power

The average charging power was defined as:

$$\langle P\rangle = \frac{W(\tau)}{\tau}, \tag{2.19}$$

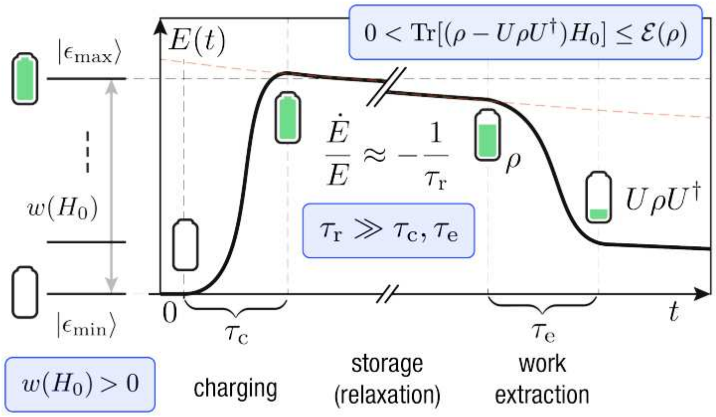

Figure 2.2: Schematic representation of a quantum battery: one can see the phases associated to the charging, storage and extraction of energy; these processes are performed with cyclic unitary operations. Futhermore, tipically, the time of the storage phase in way bigger than the other phases. Moreover the work that can be extracted has to be grater than zero and it can be, at most, like the ergotropy. In the figure one can figure out also the of the bandwidth. Image from Campioli *et al.* [6]

.

with $\langle - \rangle$ is a time average between o and τ; in other words we can write:

$$\langle P \rangle = \frac{1}{\tau} \int_0^\tau P(s) ds. \tag{2.20}$$

Binder *er al.* generalized the expression considering the family of objective functions:

$$\mathcal{P} := \langle P \rangle^\alpha \langle W \rangle^{1-\alpha} = \frac{\langle W \rangle}{T_\alpha}, \tag{2.21}$$

where T is the duration of the process and α is a free parameter such that $\alpha \in [0, 1]$ (in tha case $\alpha = 1$ we get the formula 2.19). Another interesting way to characterize the power is by defining the instantaneous power that is the time-dependent energy gain with respect to the internal QB Hamiltonian and it can be written as:

$$P(t) = \mathrm{Tr}[H_0 \left(\frac{d}{dt} \rho(t) \right)]. \tag{2.22}$$

In the following we derive a bound on the maximal energy available following Binder *er al.*[5] and Campaioli *et al.*[7].

2.3.2 Quantum speed limit time

Fisrt, we recall that the system is described by the combination of a free Hamiltonian H_0 and a time dependent one H_1; moreover the evolution of the QB state is described by the Liouville-von Neumann equation 2.3. Now we assume large fluctuations in the energy, quantified by the variance:

$$\Delta E = \sqrt{\langle H_1^2 \rangle - \langle H_1 \rangle^2} = \sqrt{\mathrm{Tr}[H_1^2 \rho] - \mathrm{Tr}[H_1 \rho]^2}. \tag{2.23}$$

Having a large variance implies that energy levels are properly distributed, and this allowed the system to transition between different eigenstates more rapidly. At this point we use the well known quantum speed limit (QSL) problem, that is a general bound on the minimum time required by a system to evolve from one state to another and, in particular, it is based on the time-energy uncertainty principle. The first example of QSL was investigated by Mandelstam and Tamm in a work published in 1945 [18]; the authors considered:

$$\partial_t A = \frac{i}{\hbar}[H, A] \quad \text{and} \quad \Delta A_t \Delta E_t \geq \frac{1}{2} \left| \langle \psi(t) | [H, A] | \psi(t) \rangle \right|, \tag{2.24}$$

where the first equation represents the evolution of the observable A and the second one shows the Robertson inequality. Now simply considering a time interval Δt we get:

$$\Delta t \Delta E \geq \frac{\hbar}{2} \frac{1}{\Delta A} \int_0^\tau dt |\partial_t \langle \psi(t)|A|\psi(t)\rangle|. \tag{2.25}$$

If we choose $A = |\psi_0\rangle\langle\psi_0|$ and we integrate over the time interval we get:

$$\Delta E \Delta t \leq \hbar \frac{\pi}{2}. \tag{2.26}$$

If we consider an initial state $|\psi_0\rangle$ and a final state $|\psi(\tau)\rangle$ orthogonal to the initial one the bounded time is:

$$\tau_{QSL} \geq \frac{\pi}{2\Delta E}; \tag{2.27}$$

the time τ_{QSL} represents precisely the shortest charging time possible. We can notice that the inverse dependence on ΔE leads to a decrease of the time as mention before. If we impose that the charging Hamiltonian have finite energy $||H_1|| = E_{max}$, the bound on the time becomes $\tau = \pi/2E_{max}$ and the charging power can be written as:

$$\langle P \rangle \leq \frac{2WE_{max}}{\pi}. \tag{2.28}$$

The formula shows that the maximal power scales with both the stored energy W and the maximum energy E_{max}

2.3.3 Quantum advantage

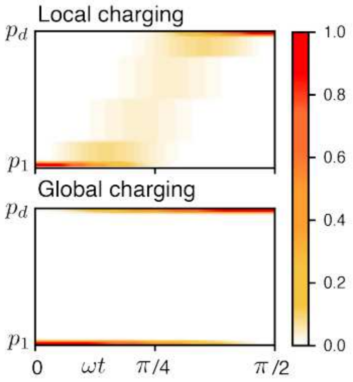

Figure 2.3: Dynamics of the population of the energy levels under different charging Hamiltonian. It is clear the difference between the local and the global charging protocol; in the second case the entanglement between the battery components decrease the distance travelled in the Hilbert space and then increase the speed of the charging. From [6]

Once the charge power is defined, it is pertinent to explore the notion of *quantum advantage*. Initially proposed by Campaioli et al. (2017)[7], quantum advantage refers to the superior performance metrics that quantum systems can exhibit over their classical counterparts. It is quantitatively expressed through the figure of merit Γ, defined as:

$$\Gamma \equiv \frac{\langle P_q \rangle}{\langle P_c \rangle} \tag{2.29}$$

where $\langle P_q \rangle$ and $\langle P_c \rangle$ are the charging power of quantum and classical charging mechanism respectively and, of course, an advantage is attained if $\Gamma > 1$.

The collective charging approach, discussed in Section 2.1.1, has a crucial importance in this context; this because during collective charging, he interactions among the N components of the battery can induce entanglement, between the different states [7]. Since this is a purely quantum phenomenon it is possible to construct the quantum advantage using a different formula:

$$\Gamma \equiv \frac{P_\sharp}{P_\parallel}. \tag{2.30}$$

Here $P_{\|}$ and $P_{\sharp}$ denote the charging powers under collective and parallel charging, respectively. The above formulation illustrates how quantum advantage is quantified by the ratio of charging power in the presence of quantum effects, such as entanglement, compared to a non-quantum (classical-like) scenario.

Nevertheless it has been shown by Campioli *et al.* is 2017 [7] that quantum advantage could be realized even in the absence of entanglement. This is achievable by optimizing the quantum coherence and correlations during the energy injection and extraction processes. In particular, minimizing energy fluctuations can increase quantum advantage without necessarily generating entanglement, thus highlighting the subtle and multifaceted nature of quantum dynamics in energy storage.

Further contributing to this discussion, Caravelli et al. [8] explored the bounds on extractable work and charging power in relation to the coherence properties of the system's density matrices. Their findings underscore the pivotal role of quantum coherence and correlations in delineating the performance limits of quantum batteries.

2.4 Quantum speed limit and quantum charging distance

We can go back and delve deeper into the concept of minimal time required for an evolution discussed in chapter 2.3.1, following the approach by Gyhm *et al.* [14]. The authors introduce the concept of quantum charging distance, which is directly related to the optimal evolution time.

Let us consider two density matrices ρ and σ with the same eigenspectra. The quantum charging distance between these states is defined as:

$$D(\rho, \sigma) = \min_{U : U\rho U^{\dagger} = \sigma} \| i \ln(U) \| , \tag{2.31}$$

where U is a unitary operator that transforms the initial state ρ and the evolved state σ. From the minimum over all the unitary operators we can extract U_{opt} which is the U that achieves the states transformation in the shortest possible time. Moreover this minimal time can be considered as the QSL time τ_{QSL} discussed in chapter 2.3.1 and it can be constructed as:

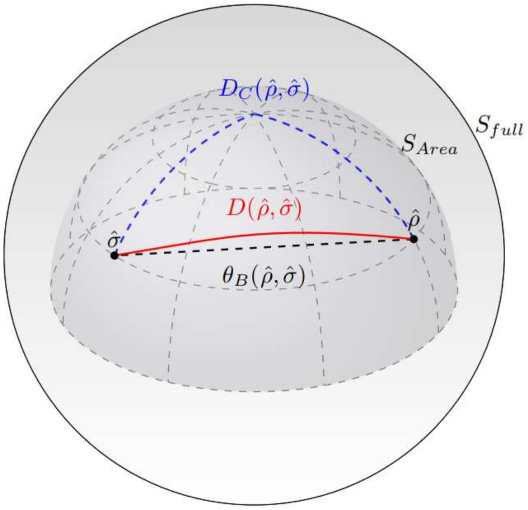

Figure 2.4: From the figure is evident that the quantum charging distance $D(\rho, \sigma)$, being defined as the shortest time necessary to a state evolution with unitary operators, is the length of the geodesic between the states in the space of their eigenspectrum. Furthermore the Bureds angle is always smaller than $D(\rho, \sigma)$. $D_C(\rho, \sigma)$ is the classical charging distance. Image form Ghym *et al.* [14]

.

$$\tau_{\text{QSL}} = \frac{\arccos |\langle \rho | \sigma \rangle|}{\min \{ \langle E \rangle, \langle \Delta E \rangle \}}. \tag{2.32}$$

In the above $\langle E \rangle$ and $\langle \Delta E \rangle$ are the time-averaged expectation value and standard deviation of energy, respectively, as defined in equation 2.23; furthermore $|\rho\rangle$ and $|\sigma\rangle$ are the states associated with the density matrices.

Knowing the charging distance is particularly useful, as it enables the application of various geometric constraints to test different models. For instance, one can define the Bures angle $\theta(\rho, \sigma)$ in terms of the fidelity $\mathcal{F}(\rho, \sigma)$ as follows:

$$\theta_B(\hat{\rho}, \hat{\sigma}) = \arccos\left[\mathcal{F}(\hat{\rho}, \hat{\sigma})\right] \quad \text{where} \quad \mathcal{F}(\rho, \sigma) = \left(\mathrm{tr}\sqrt{\sqrt{\rho}\sigma\sqrt{\rho}}\right). \tag{2.33}$$

From this, the following lower bound on the quantum charging distance can be established:

$$\theta_B(\hat{\rho}, \hat{\sigma}) \leq D(\hat{\rho}, \hat{\sigma}). \tag{2.34}$$

The Bures angle can thus be seen as the quantum charging distance in an extended Hilbert space where the states are pure. The authors also derived an upper bound for the charging distance:

$$D(\rho, \sigma) \leq \pi \left(1 - \frac{1}{d}\right). \tag{2.35}$$

Additionally, by defining the trace distance $D_{\mathrm{Tr}}(\rho, \sigma) = \frac{1}{2}\mathrm{Tr}\,|\rho - \sigma|$ one can found another interesting constraint:

$$\frac{D_{\mathrm{Tr}}(\hat{\rho}, \hat{\sigma})}{D(\hat{\rho}, \hat{\sigma})} \leq \frac{\sqrt{1 - \mathcal{F}(\hat{\rho}, \hat{\sigma})^2}}{\arccos(\mathcal{F}(\hat{\rho}, \hat{\sigma}))} \leq 1. \tag{2.36}$$

The result presented in rhis chapetr will be used in the chapter 4.4 to test our model for SYK-QB.

Chapter 3

SYK model

The Sachdev-Ye-Kitaev (SYK) model has emerged as a powerful theoretical framework for understanding a range of phenomena in quantum many-body physics, including quantum chaos, holography, and non-Fermi liquids. First proposed by Sachdev and Ye in the context of quantum spin systems, and later extended by Kitaev [2] and [1], the SYK model has become a crucial tool in exploring the connections between condensed matter physics and high-energy physics.

The SYK model's most notable feature is its solvability in the large-N limit, where N represents the number of interacting fermions. This makes it an excellent model for studying the dynamics of quantum chaos and information scrambling. The model exhibits many parallels with black hole physics, providing deep insights into AdS/CFT duality and quantum gravity. These aspects were extensively discussed in Kitaev's ”A Simple Model of Quantum Holography” and later expanded upon by Juan Maldacena and Douglas Stanford in their seminal work “Remarks on the Sachdev-Ye-Kitaev Model” [17].

The SYK model has also been extended in various directions. One notable extension is the sparse SYK model, introduced by Shenglong Xu et al. in their work ”A Sparse Model of Quantum Holography” [25]. In this variation, the interaction terms are selectively removed, reducing the computational complexity while preserving key physical properties, thus making the model more amenable to experimental realizations.

Additionally, the SYK model provides an ideal setting to explore the Eigenstate Thermalization Hypothesis (ETH), which addresses how isolated quantum systems thermalize. Sonner's work on ”Eigenstate Thermalization in the Sachdev-Ye-Kitaev Model” [24] sheds light on how thermalization emerges in this chaotic system.

Beyond its original formulation, the SYK model has been generalized to describe non-Fermi liquids, systems that do not conform to traditional Fermi-liquid theory. The paper ”Sachdev-Ye-Kitaev Models and Beyond: A Window into Non-Fermi Liquids” [10] offers an insightful review of how the SYK model helps explore these unconventional quantum states. Furthermore, the complex SYK model introduces additional features such as charge conservation, further enriching the model's ability to capture realistic quantum systems.

Together, these works form the foundation for the study of the SYK model and its variants, providing a unique lens through which to examine some of the most intriguing phenomena in modern theoretical physics.

3.1 Review of the model

The Sachdev-Ye-Kitaev model was designed as a one spatial dimension quantum-mechanical model of N Majorana fermions with a random all-to-all interaction; the Hamiltonian can be written as follows ([2] and [1]):

$$H = \frac{1}{4!} \sum_{i,j,k,l=1}^{N} J_{ijkl} \chi_i \chi_j \chi_k \chi_l. \tag{3.1}$$

Here the χ_i are the Majorana fermions which satisfy $\chi_i^\dagger = \chi_i$ and the following anti-commutation relation:

$$\{\chi_i, \chi_j^\dagger\} = \delta_{ij} \quad , \quad \{\chi_i, \chi_j\} = 0 \quad , \quad \{\chi_i^\dagger, \chi_j^\dagger\} = 0. \tag{3.2}$$

The couplings $J_{i,j,k,l}$ are taken randomly from a Gaussian distribution with zero mean and variance defined as:

$$\langle J_{ijkl} \rangle \equiv \int dJ_{ijkl} P(J_{ijkl}) = 0, \quad \langle\langle J_{ijkl}^2 \rangle\rangle \propto \frac{J^2}{N^3}. \tag{3.3}$$

Furthermore the couplings are totally antisymmetric in the indices *i, j, k, l* and the parameter J present in equation 3.3 sets the energy scale of the interaction.

Moreover we can express the real-time two-point correlation function at inverse time β:

$$G_i(t) = \langle \chi_i(t) \chi_i(0) \rangle \propto \frac{1}{\left(\beta \sinh\left(\frac{\pi t}{\beta}\right)\right)^{1/2}}, \tag{3.4}$$

where it is compute in the limit of large N and strong coupling.

The concept of *quenched disorder* plays a central role in the SYK model. In this context, the random couplings $J_{i,j,k,l}$ are fixed, or "quenched," during the computation of physical quantities. As a result, each observable in the system is dependent on a particular realization of these random couplings, and in principle, different realizations could lead to different results. However, due to the nature of quenched disorder, if the couplings are identically distributed, many physical quantities become self-averaging. This means that in the large N limit, the system behaves in such a way that these quantities converge to the same value, regardless of the specific realization of the random couplings, smoothing out the effect of disorder across the system.

3.1.1 Connection with chaos

An important characteristic of the model is that it exhibits *maximal chaos*. This can be demonstrated by analyzing the out-of-time-ordered correlator (OTOC), specifically the four-point function, which decays exponentially as:

$$\langle A(t)B(0)A(t)B(0) \rangle_\beta \sim 1 - \alpha e^{\lambda_L t_s}, \tag{3.5}$$

where α is a coefficient, λ_L is the Lyapunov exponent and t_s is the scrambling time.

The Lyapunov exponent λ_L quantifies the exponential growth of small perturbations, encapsulating the system's extreme sensitivity to initial conditions. The scrambling time t_s, which represents the timescale over which initially localized information spreads throughout the system, can be approximated as

$$t_s \sim \frac{1}{\lambda_L} \log N. \tag{3.6}$$

This timescale reflects how rapidly the system scrambles information, making it inaccessible to local measurements. In highly chaotic systems like the SYK model, the scrambling time is extremely short, indicative of fast information distribution.

The Lyapunov exponent introduced in the equation 3.5 plays a central role in characterizing quantum chaos. In an important work, Maldacena et al. [16] demonstrated that for any quantum system adhering to certain causality constraints, the Lyapunov exponent is bounded by:

$$\lambda_L \leq \frac{2\pi}{\beta}, \tag{3.7}$$

where β is the inverse temperature. As said before, the SYK model exhibits maximal chaos, which means that it saturates this bound, implying that the model scrambles information at the fastest rate permitted by quantum mechanics. As a consequence, the scrambling time in the SYK model scales logarithmically with the system size N and is given by:

$$t_s \sim \frac{\beta}{2\pi} \log N. \tag{3.8}$$

This logarithmic scaling of the scrambling time reflects the SYK model's efficiency as a fast scrambler, making it a valuable tool for studying quantum chaos and holography.

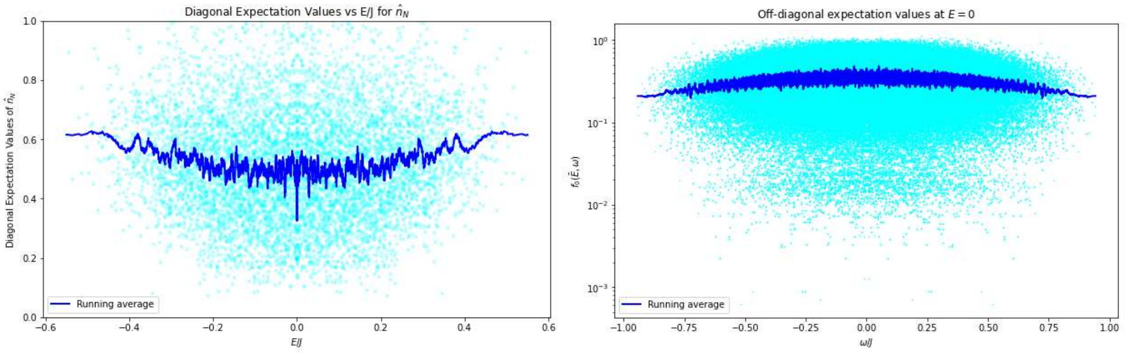

(a) On-diagonal term

(b) Off-diagonal terms

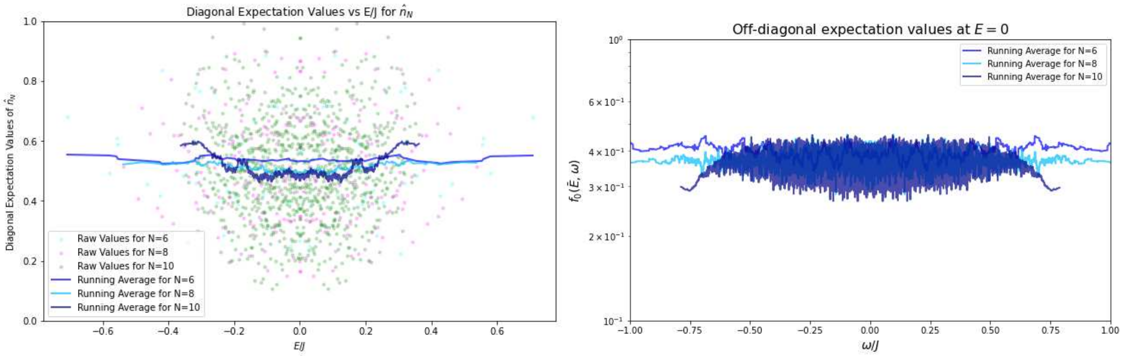

(c) On-diagonal term for 1 realization

(d) Off-diagonal terms for 1 realization

Figure 3.1: As in the figures 4.5a and 4.5b we see the stored energy and the ergotropy, in this case the model is the cSYK model.

3.1.2 Thermalization

The Eigenstate Thermalization Hypothesis (ETH) provides a framework for understanding how isolated quantum systems, starting from a non-equilibrium state, evolve toward thermal equilibrium. In essence, ETH explains why and how individual energy eigenstates of a quantum system can lead to thermal behavior, even without any external environment or reservoir.

The SYK model is particularly useful for studying the Eigenstate Thermalization Hypothesis (ETH) due to its characteristic. Indeed chaotic systems are expected to obey ETH, and the model provides a solvable test bed to explore how thermalization emerges from quantum chaos. Sonner et al. [24] explore this phenomena.

For a system satisfying ETH the matrix elements of local operators evaluated in the eigenbasis of the Hamiltonian take the form [24]:

$$\langle m|\hat{O}|n\rangle = \overline{O(\bar{E})}\delta_{mn} + e^{-S(\bar{E})/2} f_O(\bar{E}, \omega) R_{mn}, \tag{3.9}$$

where $\overline{O(\bar{E})}$ is a smooth function of the average energy $\bar{E}$, $f_O(\bar{E}, \omega)$ is a smooth function of the energy difference ω and R_{mn} is a Gaussian random variable with zero mean and unit variance. Moreover the average energy and the energy difference are expressed as:

$$\bar{E} = \frac{E_m + E_n}{2}, \quad \omega = E_m - E_n. \tag{3.10}$$

Hence the thermal behavior of certain operators is describes in terms of the properties of stationary states of the Hamiltonian since thermalization occurs in the sense of long-time averages of observables.

The nature of both the diagonal and off-diagonal components of the operator can be studied. As illustrated in the figure 3.1, we can plot the diagonal expectation values for the single-site number operator at site N for various system sizes and different numbers of disorder realizations.

Let us analyze first the on-diagonal elements which are depicted in figure 3.1a and figure 3.1c. These figures show that the expectation values of the number operator increasingly condense around a smooth limiting curve as N grows larger. This limiting curve is expected to emerge in the thermodynamic limit $N \to \infty$. To fully understand the behavior of the system, it is important to examine the relationship between the results obtained from a single disorder realization and those derived from ensemble averaging.

A key concept in this context is self-averaging: a property is said to be self-averaging if its behavior in a single realization matches that of the disorder-averaged theory. From the figures, it is evident that the Eigenstate Thermalization Hypothesis (ETH) holds in both individual realizations and in the ensemble for sufficiently large N. This convergence indicates that the ETH applies to the system in the large N-limit, as the distribution of diagonal elements aligns with the predictions of the thermal ensemble.

Let us now switch to the off-diagonal terms, presented in figure 3.1b and figure3.1d. It is evident form equation 3.9 that the off-diagonal matrix elements are suppressed by an exponential factor which depends on the thermodynamic entropy $S(\bar{E})$. Moreover the magnitude of the off-diagonal elements decays as the energy difference ω increases; in fact these elements are related to the decay of correlations over time. This suppression of long-term correlations between eigenstates ensures that the system behaves thermally. The figure shows that the off-diagonal elements become smaller in magnitude as N increases reflecting the idea that larger systems tend to thermalize more efficiently

3.2 Two point function

The two-point function plays a central role in understanding the dynamics of the SYK model. It measures the correlation between two Majorana fermions at different times, providing insight into how information propagates and decays in the system. Mathematically, the two-point function is defined as [17]:

$$G(\tau) \equiv \langle T\psi(\tau)\psi(0)\rangle = \langle \psi(\tau)\psi(0)\rangle\theta(\tau) - \langle \psi(0)\psi(\tau)\rangle\theta(-\tau) \tag{3.11}$$

where T denotes time ordering, τ is the imaginary time and ψ is a Majorana fermion. $G(\tau)$ encodes key physical properties of the system such as decay of correlations and thermalization. To build intuition, first consider the free theory (i.e., no interaction term). In this case, the two-point function is just the bare propagator of the Majorana fermions:

$$G_0(\tau) = \frac{1}{2}\text{sign}(\tau), \tag{3.12}$$

which shows that, in the free theory, the two-point function is simply a step function.

Once interactions are introduced, the two-point function $G(\tau)$ deviates from the bare propagator due to the inclusion of self-energy corrections. The situation simplifies considerably in the large-N limit, where N represents the number of interacting fermions. In this limit, the random interaction terms dominate, and the system can be described by self-consistent equations for the two-point function.

In particular, the Schwinger-Dyson equation for the two-point function $G(\tau)$ and the self-energy $\Sigma(\tau)$, that encodes the effects of interactions, can be written as:

$$G(\omega_n) = \frac{1}{i\omega_n - \Sigma(\omega_n)}, \quad \Sigma(\tau) = J^2 G^3(\tau). \tag{3.13}$$

where ω_n denotes the Matsubara frequencies. These equations can be derived using dynamical mean-field theory; however, this work will focus on a more accessible diagrammatic approach.

Let us begin by considering the bare fermion propagator, defined in equation 3.12, which takes the form $\frac{1}{2}\text{sign}(\tau)$ in imaginary time or $\frac{1}{i\omega}$ in frequency space. In the interacting picture, and specifically in the large-N limit, the SYK model is dominated by a particular class of Feynman diagrams known as melonic diagrams (as illustrated in Figure 3.2). These diagrams, which can be constructed iteratively, represent the leading-order contributions to the self-energy in this regime.

The dominance of melonic diagrams is due to their structure, which maximizes the number of independent fermion indices that can be freely summed. As a result, these diagrams contributing at the leading order in N, while non-melonic diagrams, such as cross-diagrams, introduce additional constraints on the indices, reducing the overall power of N in their contribution.

In this diagrammatic representation, each fermion propagator corresponds to a line in the diagram, and interaction vertices represent the four-fermion interaction terms. Melonic diagrams are constructed recursively, with each ”melon” corresponding to a nested or iterated self-energy correction.

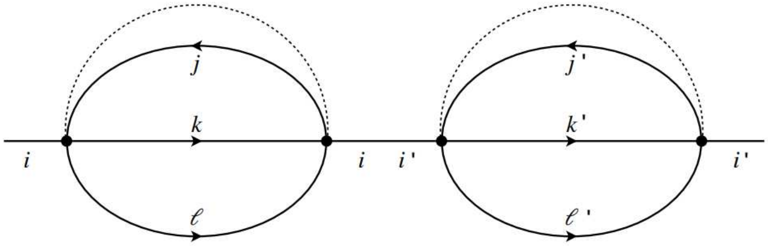

Figure 3.2: The melonic graph associared with the electron self-energy $\Sigma(\tau)$. The solid lines represent the dressed fermion propagators and the dashed line represents the disorder averaging. Adapted from Chowdhury *et al.* [10]

To derive the Schwinger-Dyson equation, one sums over all melonic diagrams that contribute to the two-point function. This procedure leads to a self-consistent equation for the two-point function and the self-energy.

3.2.1 Entropy

It is possible to write the original partition function of the theory as a functional integral of the form [17]:

$$e^{-\beta F} = \int \mathcal{D}\tilde{G}\mathcal{D}\tilde{\Sigma} \exp\left[N\left\{\log \mathrm{Pf}(\partial_t - \tilde{\Sigma}) - \frac{1}{2}\int d\tau_1 d\tau_2 \left[\tilde{\Sigma}(\tau_1,\tau_2)\tilde{G}(\tau_1,\tau_2)\right] - \frac{J^2}{q}\tilde{G}(\tau_1,\tau_2)^q\right\}\right]. \quad (3.14)$$

Here the tildes remind us that we are thinking about tge integration variables, while G and Σ without tildes are the solutions of the classical equations of motion, obeying equation 3.13. To go in details with out the goal of this work; moreover the idea to proceed is based on the fact that in the $p \to \infty$ we can know the full solutions for the G and Σ. Therefore we insert these solutions in the leading large-N approximation of equation 3.14 to get the free energy. For practical reason, it is convenient to take a derivative with respect to $J\partial_J$ of the free energy.

It has been shown ([17]) that for general q the expression of the free energy has the form:

$$\log Z = -\beta E_0 + S_0 + \frac{c}{2\beta}, \quad (3.15)$$

where E_0 is the ground-state energy, S_0 is the zero-temperature entropy and c/β is the specific heat. More precisely, the zero-temperature entropy S_0 (as the E_0 and c) is of order N and can written, from [17] and , as:

$$\frac{S_0}{N} = \frac{1}{2}\log 2 - \int_0^{\Delta} dx\, \pi\left(\frac{1}{2} - x\right)\tan \pi x \approx \frac{1}{2}\log 2 - \frac{\pi^2}{4q^2} + \dots \quad (3.16)$$

In the last the equation is approximated for large q.

3.3 Four point function

The four-point function is a fundamental tool for probing deeper aspects of the SYK model, particularly in understanding the dynamics of quantum chaos and information scrambling. While the two-point function measures the correlations between two Majorana fermions, the four-point function generalizes this concept by correlating two pairs of fermions, providing deeper insights into the system's interaction structure. Mathematically, the four-point function is defined as:

$$G_4(\tau_1,\tau_2,\tau_3,\tau_4) = \langle T\psi_i(\tau_1)\psi_j(\tau_2)\psi_i(\tau_3)\psi_j(\tau_4)\rangle, \quad (3.17)$$

where ψ are the Majorana fermion operators and τ_i (with $i \in [1,2,3,4]$) are distinct imaginary times.

The four-point function provides information about how interactions affect the fermion correlations. In particular, it plays a central role in characterizing out-of-time-ordered correlators (OTOCs), which are used to diagnose quantum chaos and information scrambling in the system. Unlike the two-point function, which captures decay and thermalization, the four-point function reveals how fermion pairs interact and how the system responds to perturbations. Specifically, in the SYK model, the four-point function exhibits exponential growth at early times, a characteristic sign of chaotic behavior, and eventually saturates due to interactions.

The averaged correlator can be written as:

$$\frac{1}{N^2}\sum_{i,j=1}^{N}\langle T(\psi_i(\tau_1)\psi_i(\tau_2)\psi_j(\tau_3)\psi_j(\tau_4))\rangle = G(\tau_{12})G(\tau_{34}) + \frac{1}{N}\mathcal{F}(\tau_1,\dots,\tau_4) + \dots \tag{3.18}$$

where $\tau_i j \equiv \tau_i - \tau_j$. This expression consists of a disconnected term, given by a product of the dressed propagators, and a connected contribution, which is subleading in $1/N$. The connected term is responsible for the quantum interactions and is described by $\mathcal{F}(\tau_1,\dots,\tau_4)$.

As in the two-point function case, we adopt a diagrammatic approach to compute the four-point function. In the large-N limit of the SYK model, the four-point function is dominated by a particular class of Feynman diagrams known as *ladder diagrams*. These diagrams play a crucial role in capturing the system's complex interactions and are responsible for encoding the chaotic behavior observed in the model.

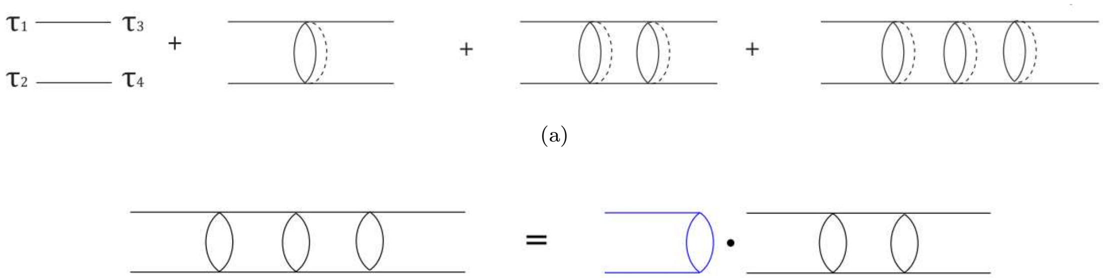

(a)

(b)

Figure 3.3: (a) shows the diagrams expressed in equation 3.18; (b) shows the general diagram $\mathcal{F}_{n+1}$ as a multiplication of the diagram $\mathcal{F}_n$ and the kernel K shown in blue. From Maldacena & Stanford [17].

Each ladder diagram consists of two two-point functions that form the "legs" of the ladder, while the interactions between fermions constitute the "rungs." The rungs correspond to the four-fermion interaction terms from the SYK Hamiltonian. The sum of ladder diagrams can be expressed as a geometric series, simplifying the computation of the four-point function.

Following the terminology of Maldacena and Stanford [17] we will denote with $\mathcal{F}_n$ the ladder with n rungs. in such a way that the "total ladder" can be written as $\mathcal{F} = \sum_n \mathcal{F}_n$. The first diagram of figure 4.9.a is simply written as:

$$\mathcal{F}_0(\tau_1,\tau_2,\tau_3,\tau_4) = -G(\tau_{13})G(\tau_{24}) + G(\tau_{14})G(\tau_{23}) \tag{3.19}$$

that is a product of propagators.

A general formula for constructing higher-order diagrams $\mathcal{F}_{n+1}$ can be derived, based on the fact that ladder diagrams are generated by successive multiplication by a kernel K. Specifically:

$$\mathcal{F}_{n+1}(\tau_1,\tau_2,\tau_3,\tau_4) = \int d\tau d\tau' K(\tau_1,\tau_2;\tau,\tau')\mathcal{F}_n(\tau,\tau',\tau_3,\tau_4), \tag{3.20}$$

where the kernel is defined as:

$$K(\tau_1,\tau_2;\tau_3,\tau_4) \equiv -J^2(q-1)G(\tau_{13})G(\tau_{24})G(\tau_{34})^{q-2}. \tag{3.21}$$

Equation 3.20 shows that the kernel K acts as a matrix operator on the sequence of ladder diagrams.

So, denoting with $\mathcal{F}_{n+1} = K\mathcal{F}_n$, we can write the sum of all ladder diagrams as a geometric series:

$$\mathcal{F} = \sum_{n=0}^{\infty}\mathcal{F}_n = \sum_{n=0}^{\infty}K^n\mathcal{F}_0 = \frac{1}{1-K}\mathcal{F}_0. \tag{3.22}$$

This final result for the four-point function is the sum of all ladder diagrams in the large-N limit and is a key ingredient in understanding the chaotic dynamics and scrambling properties of the SYK model.

3.4 Sparse SYK model

The experimental realization of the SYK model has been challenging due to the enormous number of interaction terms in the Hamiltonian. This issue has been significantly mitigated by a variant known as the sparse SYK model, introduced by Xu *et al.* [25]. In this model, interaction terms are removed from the Hamiltonian with probability $1-p$ and retained with probability p. This process can be represented by introducing a random variable $x_{i,j,k,l}$ for each coupling $J_{i,j,k,l}$ which takes the value 1 with probability p:

$$Pr(x_{i,j,k,l}=1)=p \tag{3.23}$$

and 0 otherwise. This procedure effectively reduces the number of interaction terms, as shown in the following relation:

$$L=\binom{N}{q}\approx\frac{N^q}{q!}\quad\xrightarrow{\text{sparsification}}\quad L=p\binom{N}{q}\approx p\frac{N^q}{q!}. \tag{3.24}$$

This reduction in interactions leads to the construction of a random hypergraph, as discussed in Appendix A.3. The resulting Hamiltonian for the sparse SYK model is given by:

$$H=\frac{1}{4!}\sum_{i,j,k,l}x_{ijkl}J_{ijkl}\chi_i\chi_j\chi_k\chi_l. \tag{3.25}$$

At this point, it is important to note that the energy and time scales associated with the sparse model must be comparable to those of the original SYK model (i.e with $p=1$). To ensure this comparability, the variance of the Gaussian distribution from which the couplings $J_{i,j,k,l}$ are drawn is rescaled by a factor $1/p$. Consequently, we have:

$$\langle J_{ijkl}^{\text{sparse}}\rangle=0,\quad\langle\langle J_{ijkl}^{2,\text{sparse}}\rangle\rangle=\langle\langle J_{ijkl}^2\rangle\rangle\frac{1}{p}. \tag{3.26}$$

To understand the effects of sparsification, we follow a diagrammatic analysis. In the unsparsified SYK model, the melonic diagrams contribute with a factor proportional to J^2. However, when $p\neq 1$ some differences arise. The number of configuration for which $J_{i,j,k,l}\neq 0$ is reduced by a factor of p and at the same time, the variance of the couplings is modified by the factor $1/p$. These two factors cancel each other, resulting in no net modification to the leading-order contribution.

However, in the case of iterated melonic diagrams, the situation is different. In particular, there can be terms where indices j',k',l' are permutation of j,k,l and in such cases, the diagrams contribute an additional factor of $1/p$.

On average, the number of nonzero terms in the Hamiltonian is proportional to $p\binom{N}{4}$. To characterize this, we define the parameter k as:

$$k\equiv\frac{p\binom{N}{4}}{N}\approx\frac{pN^3}{24}, \tag{3.27}$$

where k is an N-independent constant; this ensures that the number of interaction terms grows proportionally to N. Moreover, to ensure that the number of retained interactions scales linearly with the system size N, we want the average number of remaining interaction terms to satisfy $L=kN$. For this to hold, the pruning probability p must satisfy the following relation:

$$p=kN\binom{N}{q}^{-1}\approx\frac{kq!}{N^{q-1}}, \tag{3.28}$$

where k remains a positive constant. This choice of p ensures that the number of nonzero interaction terms after sparsification scales appropriately with N, thus controlling the sparsity of the model.

In the case of the sparse SYK the equations of motions can be rewrite as:

$$G_i^{\alpha\beta}(\omega)^{-1}=i\omega-\Sigma_i^{\alpha\beta}(\omega) \tag{3.29}$$

$$\Sigma_{i_1}^{\alpha\beta}=\langle J^2\rangle\sum_{i_2<\cdots<i_q}x_{i_1i_2\ldots i_q}G_{i_2}^{\alpha\beta}\cdots G_{i_q}^{\alpha\beta} \tag{3.30}$$

where $I\equiv i_1\ldots i_q$ is the collective index. In this case we can not take the limit $N\to\infty$ (since the action does not depend explicitly on N): this means that the fluctuations around the saddle point may be an important contribution to consider.

3.5 Complex SYK model

For most of the discussions outlined in Chapter 4, the model introduced in Chapter 3 will not be employed; instead, a variant of the original model will be utilized, the so called *complex SYK model* (c-SYK) that is a generalization of the standard model involving complex fermions. The new Hamiltonian is [13]:

$$H = \sum_{i,j,k,l}^{N} J_{ij;kl} c_i^\dagger c_j^\dagger c_k c_l \tag{3.31}$$

where the couplings $J_{i,j,k,l}$ are complex parameters and the fermion creation and annilihation operators $c_i^\dagger$ and c_i satisfy $\{c_i, c_j^\dagger\} = \delta_{ij}$ and $\{c_i, c_j\} = \{c_i^\dagger, c_j^\dagger\} = 0$. Moreover the antisymmetry and hermiticity of the system are guarantied by the constraints:

$$J_{ij;kl} = -J_{ji;kl}, \quad J_{ij;kl} = -J_{ij;lk}, \quad J_{ij;kl} = J^*_{kl;ij}. \tag{3.32}$$

3.6 Relation between quantum chaos and sparsity

In this chapter, we explore the impact of sparsity on quantum chaos within the SYK model. To achieve this, we will follow the approach presented by Orman *et al.* [19], focusing on two key quantities that characterize the eigenvalue spectrum: the Spectral Form Factor (SFF) and the nearest-neighbor eigenvalue gap ratio. These measures provide insights into the quantum chaos manifestation in the system and facilitate an exploration of how sparsity influences the dynamical properties relevant to quantum battery performance.

The inherently chaotic nature of the SYK model is evident in its energy eigenvalue spectrum, which aligns closely with predictions from random matrix theory (RMT). A more detailed exposition of RMT is reserved for the Appendix A.4; here, we summarize the key concepts necessary for our analysis.

Let us introduce the eigenvalues of a general matrix M denoted as $\{E_i\}$ and a general normalized eigenvalue density $\rho(E)$, with its average given by $\langle \rho(E) \rangle$. The correlations among the eigenvalues are captured by the eigenvalue pair correlation function defined as $R(E_1, E_2) \equiv \langle \rho(E_1)\rho(E_2) \rangle$. Analyzing it, and in particular the energy difference $|E_1 - E_2|$, it is possible to extract interesting properties.

If the energy difference is large compared to the mean spacing between the eigenvalues, the correlation function's amplitude decreases inversely with the square of the distance $1/x^2$. This damping of long-range fluctuations in the eigenvalue distribution is called "spectral rigidity". Spectral rigidity is observed when the difference in energy between pairs of eigenvalues, $|E_1 - E_2|$, is less than a characteristic scale known as the Thouless energy. Beyond this scale, where $|E_1 - E_2|$ exceeds the Thouless energy, the assumption of spectral rigidity no longer holds, leading to a breakdown in the predictive power of this model.

3.6.1 Spectral form factor and nearest-neighbor gap ratio

The spectral form factor provides a robust measure of spectral rigidity and it is commonly defined in terms of the analytically continued partition function as follows [24]:

$$SFF(\beta, t) \equiv \frac{\langle Z(\beta + it) Z(\beta - it) \rangle}{\langle Z(\beta)^2 \rangle}, \tag{3.33}$$

where β is the inverse temperature. In this chapter we analyze the SFF using the strategy introduced in Gharibyan et al. [11], which employs a microcanonical ensemble refined by a Gaussian window. This modification mitigates the non-universal spectral features that typically induce significant oscillations in the SFF near the ramp. Accordingly, we introduce the following function:

$$|Y(\alpha, t)|^2 = \left| \sum_i e^{-\alpha E_i^2} e^{-iE_i t} \right|^2, \tag{3.34}$$

and subsequently define:

$$h(\alpha, t) = \left\langle \frac{|Y(\alpha, t)|^2}{|Y(\alpha, 0)|^2} \right\rangle, \tag{3.35}$$

where α serves as a filtering parameter that controls the Gaussian width, effectively smoothing fluctuations in the spectral data.

To fully appreciate the role of the Spectral Form Factor (SFF), we can consider it as a measure of how well the energy levels of a system, spread over a certain range, adhere to expected statistical distributions derived from Random Matrix Theory. In practical terms, the SFF provides insights into how changes in sparsity within the SYK model might modify the energy level distributions, thus potentially impacting the system's manifestation of quantum chaos. This, in turn, can affect how quantum batteries, which rely on these principles, perform and operate.

The figure 3.4a show the filtered SFF in the case of $N = 26$ (from Orman et al. [19] and figure 3.4b show the filtered SFF for N=6.

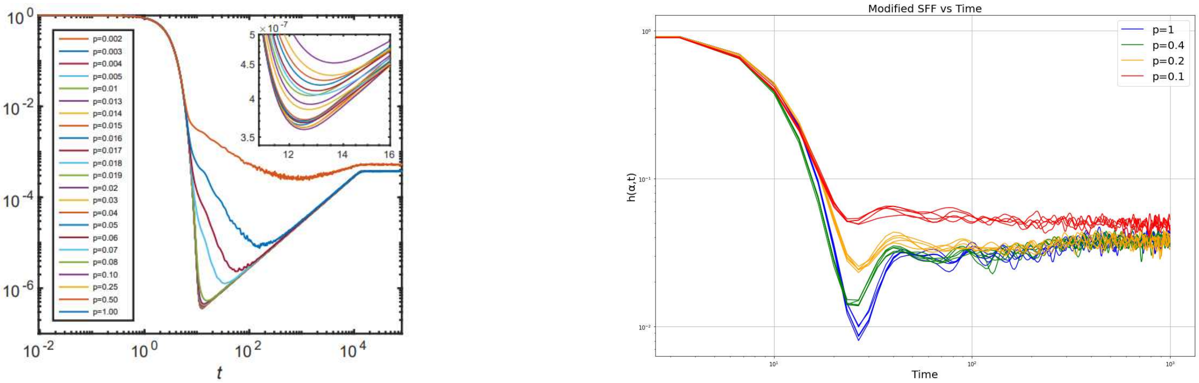

(a) SFF for N=26

(b) SFF for N=6

Figure 3.4: SFF for N=26 as a function of the time for different value of the sparsity parameter p (a) form Orman et al. [19] (a). SFF for N=6 for the sparsity parameter p equals to 1, 0.4, 0.2 and 0.1 (b).

Another important quantity for our analysis is the nearest-neighbor gap ratio r defined as the average over the spectrum of the ratios of two successive eigenvalue gaps. It can be expressed as follows:

$$r = \left\langle \min\left(\frac{s_i}{s_{i+1}}, \frac{s_{i+1}}{s_i}\right)\right\rangle_i = \left\langle \min\left(\frac{E_i - E_{i-1}}{E_{i+1} - E_i}, \frac{E_{i+1} - E_i}{E_i - E_{i-1}}\right)\right\rangle_i, \tag{3.36}$$

where $s_i = E_i - E_{i-1}$ is the interval between consecutive eigenvalues. As previously mentioned, in systems that exhibit quantum chaos, the distribution of these gap ratios typically aligns with predictions from Random Matrix Theory providing a robust framework for understanding the statistical properties of the eigenvalues .

3.6.2 The transition point p_1

The transition point p_1 is denoted as the largest value of p for which the SFF of the sparse model significantly deviates from the spectral form factor of the unsparsified model. In order to calculate this point we need to introduce the relative error at the onset of the ramp defined as:

$$\text{relative error} = \frac{\min YY_p^*}{\min YY_{p=1}^*}, \tag{3.37}$$

with Y defined as before.

Following Orman *et al.* we define p_1 as as the value of p for which the relative error is 1.2. What is significant is that for $p < p_1$ the SFF deviates significantly from its behavior for $p = 1$, signaling that in this regime the sparsified model is less strongly chaotic than the unsparsified model. In figure 3.5b found the value of p_1 for $N = 6$ and $N = 8$, respectively $p_1 = 0.5367$ and $p_1 = 0.4750$.

Orman et al. found that the distribution of p_1 as a function of N can be reproduced by the fucntion:

$$p_1 = \frac{k_1 N}{\binom{N}{4}} \approx \frac{24 k_1}{N^3} \tag{3.38}$$

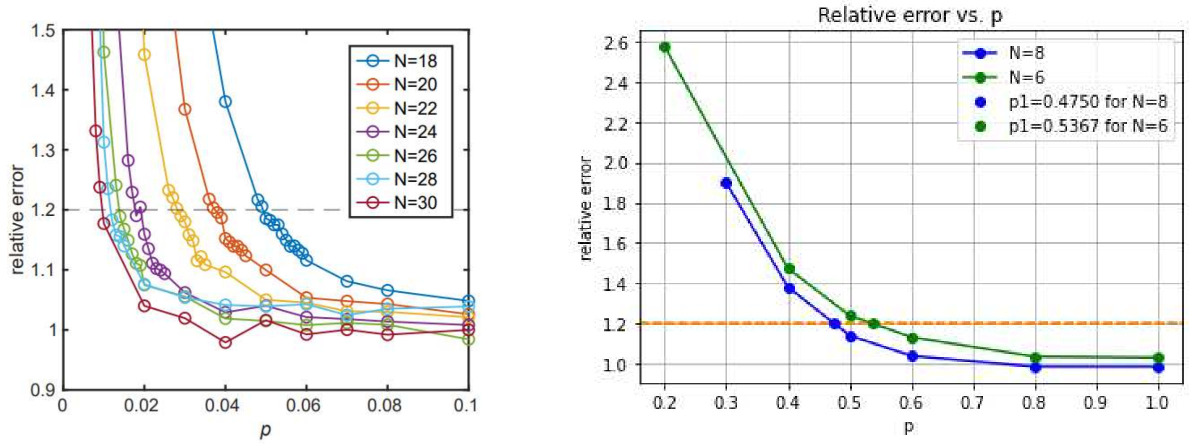

(a) reference figure (b) calculated figure

Figure 3.5: Relative error vs p form Orman *et al.* [19] and the same for N=8.

where $k_1 = 8.7$ is a constant interpret as the average degree of the interaction for sparsity p_1. It is evident that our results are not in agreement whit the fit; moreover if we consider $N = 4$ and equation 3.38 one get that $p_1 \equiv 3.2625$ which is clearly implausible. The equation 3.38 was obtained by fitting results for $N \geq 18$ and it is plausible to think that for small N the behavior could be different.

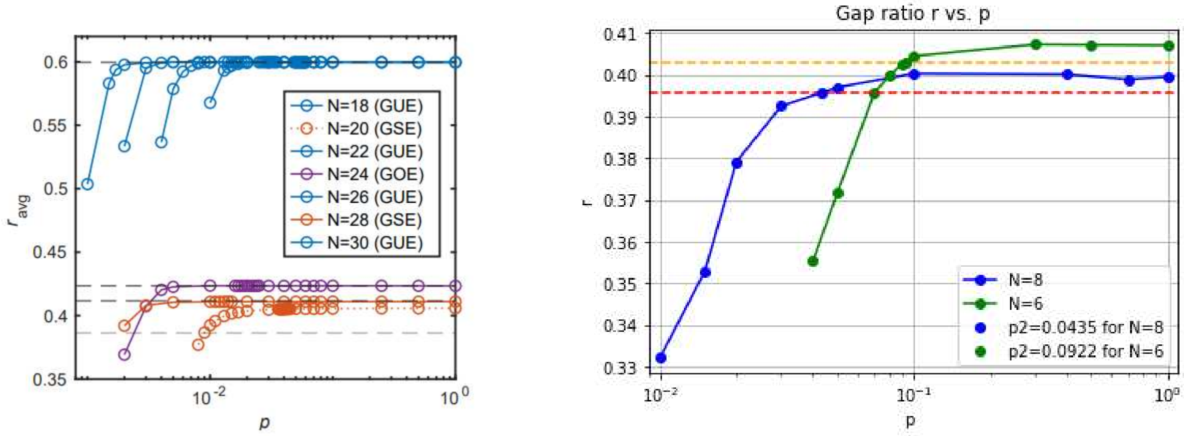

(a) reference figure (b) calculated figure

Figure 3.6: Gap ratio r vs p form Orman *et al.* [19] and the same for N=8.

3.6.3 The transition point p_2

Another critical transition point, denoted as p_2,can be defined where the gap ratio r diverges from the predictions of Random Matrix Theory (RMT), marking a significant loss of spectral rigidity. Specifically, at p_2, the characteristic 'ramp' feature in spectral statistics vanishes entirely, highlighting a significant shift in eigenvalue dynamics. Given the challenges in pinpointing p_2 precisely from Spectral Form Factor (SFF) plots due to their complexity, an alternative metric is employed: the eigenvalue gap ratio r. This metric, indicative of eigenvalue repulsion at scales comparable to the average eigenvalue spacing, remains stable under sparsification until p decreases to p_2. At this juncture, a sharp decline in r is observed, signaling the collapse of spectral rigidity at smaller energy difference scales.

To be concreate, p_2 is defined as the value of the sparsity parameter for which r reaches the 99% of its value in the unsparsified case. The results for the p_2 values are shown in figure 3.6b and they corresponds to $p_2 = 0.0922$ for $N = 6$ and $p_2 = 0.0435$ for $N = 8$.

As before Orman et al. found that the this transition point and N are connected via the equation:

$$p_2 = \frac{k_2 N}{\binom{N}{4}} \approx \frac{24 k_2}{N^3} \tag{3.39}$$

where $k_2 \approx 2.3$ is a constant that is interpreted as the average degree of the interaction for sparsity p_2. We see again that our results are not in agreement with the with the prediction but similar consideration can be done.

Therefore combining the two results one can conclude that the rigidity of the eigenvalue spectrum matches that of the unsparsified model when $p > p_1$, that it deviates from the unsparsified model when energy differences are large for $p_1 < p < p_2$ and that it deviates significantly even for small energy differences for $p < p_2$.

Chapter 4

SYK quantum batteries analysis

Quantum batteries are a rapidly growing field of research, focusing on how quantum systems can be harnessed to store and deliver energy with potentially superior performance compared to classical batteries. Among the various models studied in this field, the Sachdev-Ye-Kitaev (SYK) model has emerged as a powerful theoretical tool for understanding the dynamics of many-body quantum systems. Its unique properties (including strong correlations, quantum chaos, and all-to-all interactions) make the SYK model an intriguing candidate for exploring optimal quantum battery dynamics.

The SYK model offers a highly intriguing framework for studying quantum batteries. Its solvability in the large-N limit and its chaotic dynamics make it an ideal platform for exploring the optimal charging and discharging processes in a quantum battery. The model exhibits fast scrambling of quantum information, a property shared with black holes, making it a particularly efficient system for distributing energy across its degrees of freedom.

In this chapter, we will explore how the SYK model can be applied to the study of quantum batteries-guided by recent theoretical advancements and numerical analyses. Specifically: (1) we will investigate the evolution of energy-level populations within the SYK quantum battery, building on the work of Rossini*et al.* [22], and this gives insight into how energy states are occupied and distributed over time; (2) we will investigate how the model's chaotic dynamics contribute to maximizing the power output, and how this aligns with theoretical bounds on power; (3)we will verify the bounds on the quantum charging distance as defined in Gyhm *et al.* [14]; (4) we will explore the time evolution of ergotropy in the SYK quantum battery, following the studies by Hoang *et al.* [15], in order to quantify the battery's performance and efficiency; (5) we will study the charging stability (Rosa *et al.* [21] and Rossini *et al.* [22]) of the SYK model with respect to different models and we will quantify the different types of fluctuations responsible for the istabilities.

4.1 SYK Quantum Batteries

As mentioned in equation 2.8 a quantum battery (QB) can be described as N quantum cells, each acting as an individual unit of energy storage. The Hamiltonian governing the system can be written as $H_0 = \sum_{i=1}^{\mathrm{N}} h_i$. In the case of a SYK quantum battery [23] we assume that each constituents of the battery is a spin-1/2 system and the Hamiltonian can be written as follows:

$$H_0 = \sum_{i=0}^{N} \omega_0 \sigma_i^y, \tag{4.1}$$

where $\omega_0 > 0$ represents a magnetic field strength and σ_i^y is the Pauli matrix for the y direction. The Hamiltonian H_0 is local and free, implying that it does not involve interactions between different spins; instead, each spin interacts independently with the magnetic field.

For the charging Hamiltonian we consider an SYK model, more precisely the complex Sachdev–Ye–Kitaev model (c-SYK), an ensemble of $q = 4$ fermionic interactions that provides a non-local, strongly correlated charging Hamiltonian:

$$H_1 = H_{\text{c-SYK}} = \sum_{i,j,k,l=1}^{N} J_{i,j,k,l} \hat{c}_i^\dagger \hat{c}_j^\dagger \hat{c}_k \hat{c}_l. \tag{4.2}$$

Here $\hat{c}_i^\dagger$ and $\hat{c}_1$ are the spinless fermionic creation and annihilation operators, for a system of spinless fermions. These operators are constructed using the Jordan-Wigner transformation:

$$\hat{c}_j^\dagger = \hat{\sigma}_j^+ \left(\prod_{m=1}^{j-1} \hat{\sigma}_m^z \right) \quad \text{where} \quad \hat{\sigma}_j^\pm \equiv \frac{\hat{\sigma}_j^x \pm i\hat{\sigma}_j^y}{2}, \tag{4.3}$$

where $\hat{\sigma}_j^\pm$ denote the ladder operators for spin at site j.

The couplings $J_{i,j,k,l}$ are zero-mean Gaussian-distributed complex random variables with variance $\langle\langle J_{i,j,k,l}^2 \rangle\rangle$ and properties defined as follows:

$$\langle\langle J_{i,j,k,l}^2 \rangle\rangle = 3! \frac{J^2}{N^3} \tag{4.4}$$

$$J_{i,j,k,l} = J_{k,l,i,j}^*, \quad J_{i,j,k,l} = -J_{j,i,k,l} = -J_{i,j,l,k}. \tag{4.5}$$

The notation $\langle\langle \mathcal{O} \rangle\rangle$ for any operator $\mathcal{O}$ is defined as:

$$\langle\langle \mathcal{O} \rangle\rangle \equiv \int P(\{J_{i,j,k,l}\}) \mathcal{O}(\{J_{i,j,k,l}\}) d\{J_{i,j,k,l}\} \tag{4.6}$$

where $P(\{J_{i,j,k,l}\})$s the probability distribution for the coupling constants. The equation represents the average of different realization of the coupling $J_{i,j,k,l}$; from an operational point of view this can be translate in a average over different realization of the charging Hamiltonian H_1.

A fundamental characteristic of the QB system is the non-commutativity between the Hamiltonians H_0 and H_1:

$$[H_0, H_1] \neq 0. \tag{4.7}$$

This condition is essential for energy transfer between the charging Hamiltonian and the quantum battery Hamiltonian in fact non-commutativity implies that H_1 induces transitions between different eigenstates of H_0, allowing energy injection into the system, a necessary condition for the charging process.

In summary, the SYK quantum battery is governed by a local and free Hamiltonian H_0 and by a on-local, strongly correlated charging Hamiltonian $H_1 = H_{\text{c-SYK}}$.

4.1.1 Charging protocol

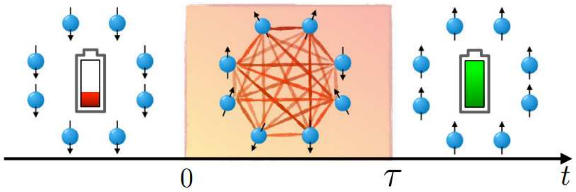

Figure 4.1: Charging of a SYK quantum battery. The system, made of N spin-1/2 components, evolve after the all-to-all interaction driven by H_1 from the all spin-down configuration to the all spin-up one. The energy injection is computed during a time interval $0 < t < \tau$. at the and of the charging the battery has a stored energy $W(\tau)$. From [23]

.

At time $t = 0$ the system is prepared in the ground state of the quantum battery Hamiltonian $|\psi_0\rangle = |0\rangle$. The charging process is generated by the interaction between H_0 and the charging Hamiltonian H_1 at least for a time $t \neq 0$. More precisely the Hamiltonian describing the total system can be written as:

$$H(t) = H_0 + \lambda(t) H_1, \tag{4.8}$$

where $\lambda(t)$ is a parameter which can be described as a step function with the value equal to 1 for $t \in [0, \tau]$ and zero elsewhere; for this reason the function λ represents an external control on the system and it modulates the interaction between the charger and the battery. For the time evolution of the state we will use the notation

$$|\psi(t)\rangle = e^{-itH(t)} |\psi_0\rangle. \tag{4.9}$$

The charging protocol for an SYK quantum battery is depicted in Figure 4.1. The system, consisting of N spin-1/2 components, evolves under an all-to-all interaction led by H_1, transitioning from the initial all spin-down state to a highly excited state, such as the all spin-up configuration. The energy tranfer occurs over the whole interval fro 0 to τ resulting in a stored energy $W(\tau)$ at the end of the charging period.

4.2 Population dynamics

A deeper understanding of the system's behavior can be gained by analyzing the time evolution of the energy-level occupations. We consider the Hamiltonian in equation 2.1 and we assume the eigenvalues to be denoted by $\epsilon_k = k\omega_0$ where ω_0 is the characteristic energy scale. The dynamics of the populations of each energy level k can be written as follows [23]:

$$p_k(\tau) = \sum_k |\langle k|\psi(\tau)\rangle|^2, \tag{4.10}$$

where $|\psi(\tau)\rangle$ represents the time-evolved quantum state at time τ and $p_k(\tau)$ gives the probability that the system occupies the energy level k at time τ.

Figure 4.2 show the population dynamics for the c-SYK. The dynamics exhibit a distinctly non-local character, as discussed by Rossini *et al.*[23] In particular, one observe two primary phases. In the initial phase, a short thermalization process takes place, during which the system reaches a quasi-equilibrium state. Following this, we observe a second phase, where the excitations are no longer confined to a particular region of the energy spectrum. Instead, the excitations spread across the entire set of energy levels, indicating that the system explores a broad portion of the Hilbert space.

This behavior is a hallmark of systems with strong all-to-all interactions where the lack of localization in energy space allows for efficient thermalization and the rapid spread of information throughout the system.

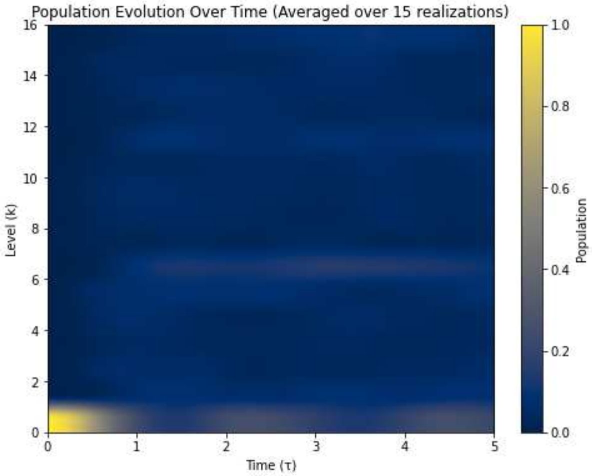

Figure 4.2: Dynamic of the population of the energy levels of the SYK quantum batteries as a function of the time.

.

4.3 Bounds on power

Following Rossini et al. [23] it is possible to obtain quantitative results on the charging performances of the battery. The authors investigated the quantum advantage of the SYK model using the following bound:

$$P_N(\tau) \leq 2\sqrt{\Delta_\tau \hat{H}_0^2 \Delta_\tau \hat{H}_1^2}, \tag{4.11}$$

where we define the following:

$$\Delta_\tau \hat{H}^2 \equiv \left(\frac{1}{\tau}\right)\int_0^\tau dt\left[\langle \hat{H}^2\rangle_t - \left(\langle\hat{H}\rangle_t\right)^2\right], \tag{4.12}$$

and ,in this context, $\Delta_\tau \hat{H}_1{}^2$ is related to the charging speed in the Hilbert space.

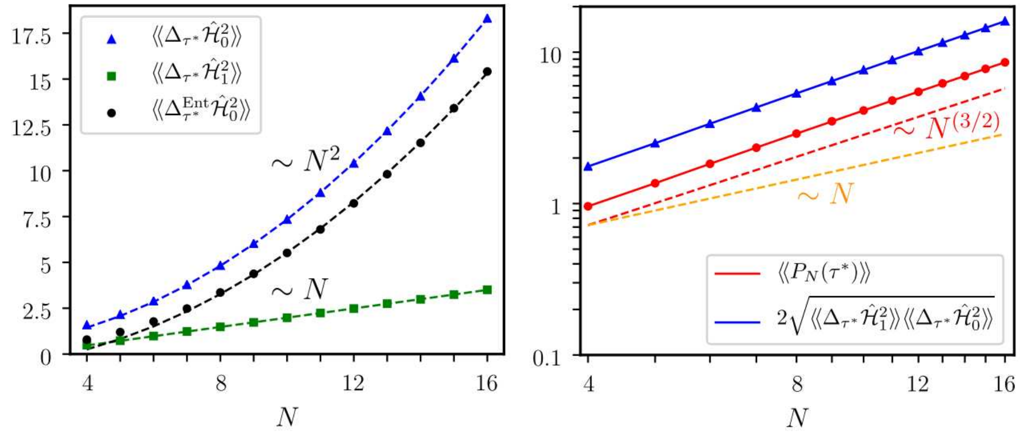

Figure 4.3: In the first image time-averaged variances $\langle\Delta_\tau\hat{H}_0^2\rangle$ (blue triangles, in units of ω_0^2), $\langle\Delta_\tau\hat{H}_1^2\rangle$ (green squares, in units of J^2), and $\langle\Delta_\tau^{\text{ent}}\hat{H}_0^2\rangle$ (black circles, in units of ω_0^2) are plotted as functions of N.In the second figure the optimal power $\langle P_N(\tau)\rangle$ (red) and the quantity on the right-hand side of the power bound (blue) are plotted as functions of N on a log-log scale, in units of $\omega_0 J$. Images from Rossini *er al.* [23].

On the other and $\Delta_\tau \hat{H}_0{}^2$ represents the distance travelled in the Hilbert space and an increase in this distance can be seen as a formation of a "shortcuts". Therefore, as discussed in chapter 2.3.3, considering entangled states it is possible to reduced the distance travelled in the Hilbert space. For this reason an enhancement of $\Delta_\tau \hat{H}_0{}^2$ can be linked to a genuine quantum advantage. Moreover if the QB Hamiltonian is made of a sum of local terms we can write $\Delta_\tau\hat{H}_0^2$ as a sum of the following contributes:

$$\Delta_\tau^{\text{loc}}\hat{H}_0^2 = \frac{1}{\tau}\int_0^\tau dt \sum_i \left(\langle(\omega_0\sigma_i^y)^2\rangle_t - \langle\omega_0\sigma_i^y\rangle_t^2\right), \tag{4.13}$$

$$\Delta_\tau^{\text{ent}}\hat{H}_0^2 = \frac{1}{\tau}\int_0^\tau dt\sum_{i\neq j}\left(\langle\omega_0\sigma_i^y\omega_0\sigma_j^y\rangle_t - \langle\omega_0\sigma_i^y\rangle_t\langle\omega_0\sigma_j^y\rangle_t\right). \tag{4.14}$$

The first term consists of local contributions and therefore scales linearly with N, whereas the second term, which captures the correlations between sites i and j, exhibits a superlinear dependence on N.

Now from equation 4.11, considering the average over different realization of the coupling $J_{i,j,k,l}$, it is possible to extract the following bound:

$$\langle\langle P_N(\tau^*)\rangle\rangle \le 2\sqrt{\left\langle\left\langle \Delta_{\tau^*}\hat{H}_0^2\right\rangle\right\rangle\left\langle\left\langle\Delta_{\tau^*}\hat{H}_1^2\right\rangle\right\rangle}. \tag{4.15}$$

where we are interest to study it at the time $\tau*$ that is the optimal time at which the power is maximum.

Empirical results from Rossini *et al.* indicate that the maximum power $\langle\langle P_N(\tau^*)\rangle\rangle$ and the quantum fluctuations $\Delta_\tau\hat{H}0^2$ and $\Delta\tau\hat{H}_1^2$ show scaling behaviors that are dependent on the system size N. Notably, the maximum power scales superlinearly with N, following a $N^{3/2}$ trend, highlighting the quantum advantage enabled by the chaotic dynamics and strong correlations inherent in the SYK model. These results suggest that the SYK model's unique properties significantly enhance charging power and efficiency, showing an advantage with respect to classical strategies and illustrating the potential of exploiting quantum chaos in technological applications such as energy storage.

4.4 Charging quantum distance and time

In this chapter, we evaluate the quantum charging distance $D(\rho, \sigma)$, Bures angle $\theta_B(\rho, \sigma)$, trace distance $D_{Tr}(\rho, \sigma)$ and quantum speed limit time τ_{QSL} for a SYK model with $N = 8$, $J = 5$ and $\omega_0 = 1$. The results are presented in table 4.1 and we can chack if the bounds established in in chapter 2.4.

Charging distance $D(\rho, \sigma)$	Bures angle $\theta_B(\rho, \sigma)$	Trace distance $D_{Tr}(\rho, \sigma)$	QSL time τ_{QSL}
1.1960	0.0848	0.1236	0.3134

Table 4.1: Value obtained for $N = 8$, $J = 5$ and $\omega_0 = 1$

First we can consider that the Bures angle $\theta_B(\rho, \sigma)$ provides a lower bound for the quantum charging distance, given by $\theta_B(\rho, \sigma) \leq D(\rho, \sigma)$. From table 4.1 we see that $\theta_B(\rho, \sigma) = 0.0848$ and $D(\rho, \sigma) = 1.1960$, satisfying this inequality.

Moreover an upper bound for the charging distance is given by $D(\rho, \sigma) \leq \pi\,(1 - 1/d)$ where d is the Hilbert space dimension and this results is in agreement with the value of the table.

Finally, even the trace distance can be used to bound the charging distance through the inequality shown in equation 2.36. With $D_{Tr}(\rho, \sigma) = 0.1236$ and $D(\rho, \sigma) = 1.1960$ this condition is also satisfied, indicating that the system's trace distance lies within the expected bounds.

The results confirm that the bounds on the quantum charging distance are respected under the chosen parameters and reinforce the consistency of the model with the theoretical constraints on quantum evolution.

4.5 Time evolution and ergotropy

For the study of the ergotropy and its time evolution we will compare our data with Hoang et al. [15] in order to have a confirmation of the validity of the used time evolution. The authors based their study on the variational quantum ergotropy (VQErgo) algorithm which can be divided in four steps.

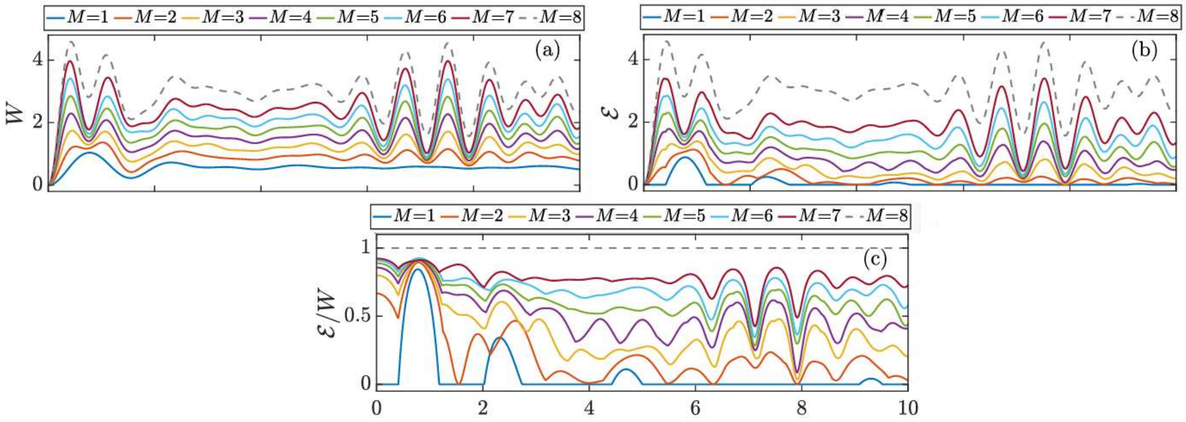

Figure 4.4: Stored energy W (a), ergotropy $\mathcal{E}$ and ratio $\mathcal{E}/W$ that is the battery efficiency for different value of M from 1 to $N = 8$. This graph is obtained with a time evolution based on the Suzuki-Trotter decomposition.From Hoang *et al.*[15]

.

The battery is initially prepared in an uncharged state, which can be any arbitrary state; however, as discussed in chapter 4.1.1, we specifically use the ground state of the quantum battery Hamiltonian H_0. For the charging process, the system is evolved in time under the charging Hamiltonian H_1 for the required duration. While the original authors employed the Trotter-Suzuki decomposition to approximate the unitary time evolution operator e^{-itH_1}, we opted for an alternative approach using the Lindblad master equation for directly compute the evolution.

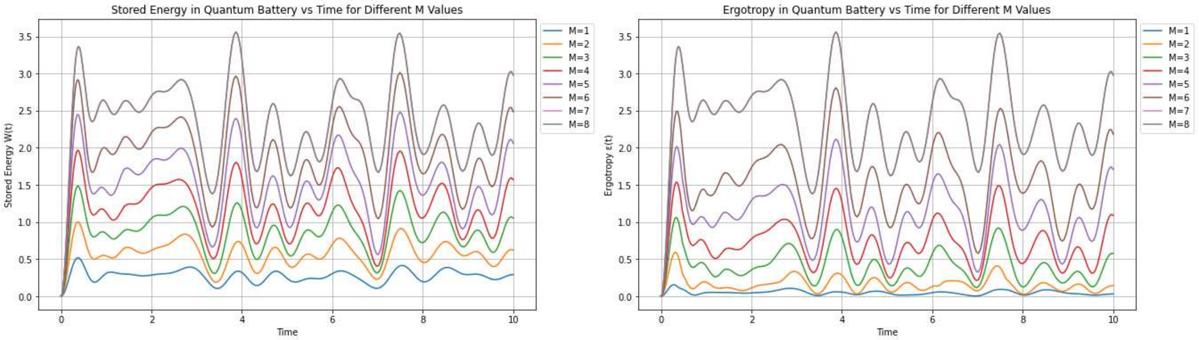

(a) stored energy

(b) ergotropy

Figure 4.5: The stored energy and the ergotropy for the same spin model used in the figure 4.4 but with a differnet time evolution. In this case we did not evolve the system with the Suzuki-Trotter decomposition based method.

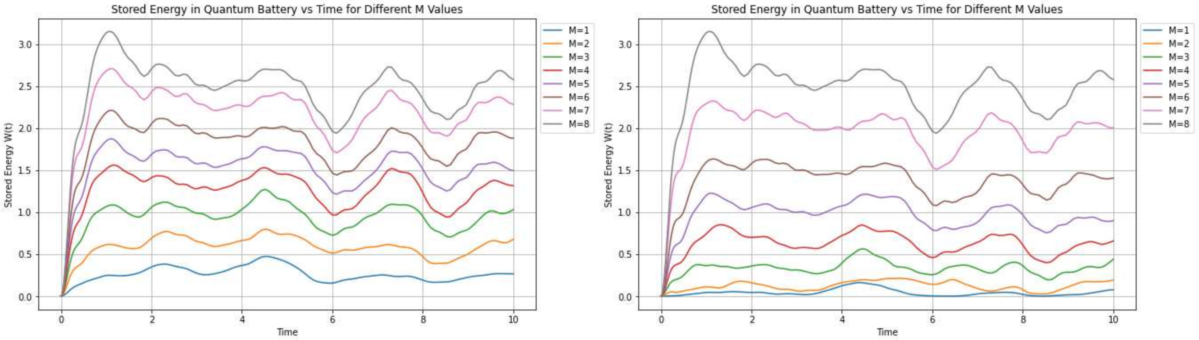

(a) stored energy

(b) ergotropy

Figure 4.6: as in the figures 4.5a and 4.5b we see the stored energy and the ergotropy, in this case the model is the cSYK model.

The Lindblad master equation is an extension of the Liouville-von Neumann equation that allows for the inclusion of non-unitary processes, making it suitable for modeling open quantum systems:

$$\frac{d}{dt}\rho(t) = -i[H, \rho(t)] + \sum_k \left(L_k \rho(t) L_k^\dagger - \frac{1}{2}\{L_k^\dagger L_k, \rho(t)\} \right), \tag{4.16}$$

where L_k are collapse operators representing dissipative effects such as energy loss due to absorption and decoherence; therefore this formalism enables the simulation of realistic scenarios where the quantum battery experiences energy dissipation.

At this point the ergotropy is calculated as the difference of mean energy and passive energy (as show in equations 2.10 and 2.11) considering a subsystem of $M < N$ battery constituents. In particular the mean energy can be written as:

$$W_{\text{mean}} = \langle \psi(t) | H_0^M \otimes I^{\otimes(N-M)} | \psi(t) \rangle, \tag{4.17}$$

while the passive energy is written as:

$$W_{\text{passive}} = \min_U \left[\langle \psi(t) | \left(U^\dagger H_0^M U \right) \otimes I^{\otimes(N-M)} | \psi(t) \rangle \right]. \tag{4.18}$$

The final result can be easily computed with the formula 2.15 on the subsystem of M units.

Before proceeding with the study of the ergotropy calculation for the SYK battery it is crucial to check if the time evolution (based on the Lindblad master equation) used by us is safely applicable. With

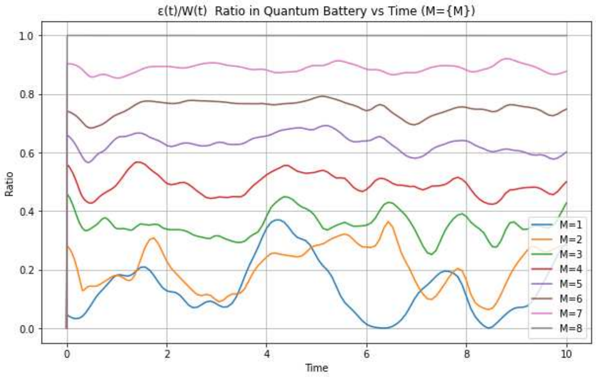

Figure 4.7: The efficiency of the battery $\mathcal{E}/W$ fro the cSYK model as a function of the charging time t for different values of the M parameter.

.

this aim we tried to reproduced the results of Hoang et al. [15] and than checked for any substantial errors. We reproduced the spin-chain model:

$$H_0 = -h \sum_{i=1}^{N} \sigma_i^z \quad \text{and} \quad H_1 = -h \sum_{i=1}^{N} \sigma_i^z - J \sum_{i=1}^{N-1} \sigma_i^x \sigma_{i+1}^x, \tag{4.19}$$

and prepared the initial state with the ground state $|\psi(t=0)\rangle = |0\rangle^{\otimes N}$.

Figure 4.4 show the Trotter-Suzuki decomposition result from Hoang et al. [15] while figures 4.5 show the result for the Lindblad master equation evolution. Overall the physical aspects of the system seem to be well conserved between the two; in particular we recognize periodicity and energy revivals typical of coherent evolution. Furthermore the scaling of the stored energy with the number of sub-units M is conserved between the two plots, with higher M values having higher stored energy peaks.

Figures 4.6a, 4.6b and 4.7, on the other hand, show the stored energy, ergotropy and battery efficiency for the SYK model. Compared to the spin chain model described in equation 4.19, the chaotic model exhibits significantly greater stability. While a more detailed analysis of this stability will be presented in chapter 4.6, some preliminary observations can be made. A key difference between the two models lies in the all-to-all interaction structure of the SYK model. This interaction pattern facilitates a rapid spread of correlations and energy throughout the system, which minimizes localized fluctuations and promotes a more uniform distribution of energy. This behavior is closely linked to the fast scrambling properties of the SYK model, where information and energy are quickly dispersed across the entire system.

4.6 Charging stability

For the study of the charging stability in quantum batteries we consider a protocol similar to the one outlined in equation 4.1.1, plus the introduction of a dimensionless parameter which controls the relative strength between the QB and the charging Hamiltonian k:

$$H(t) = H_0 + k\lambda(t)H_1. \tag{4.20}$$

Rosa *et al.* [21] provided a solid way to analyze the performance of the charging protocol, identifying the fluctuations responsible for limiting the energy storage capacity and affecting the efficiency of the charging process.

Three primary types of fluctuations are identified: temporal fluctuations, disorder fluctuations, and quantum fluctuations. *Temporal fluctuations*, defined as the fluctuations in stored energy over a given time interval, are quantified by:

$$\left[\sigma_N^{(t)}(\tau_{\max})\right]^2 \equiv \left\langle\left\langle \left[\int_0^{\tau_{\max}} \frac{1}{\tau_{\max}} d\tau \langle H_0\rangle_\tau^2\right] - \overline{W}^2(\tau_{\max}) \right\rangle\right\rangle. \tag{4.21}$$

Here the quantity $\overline{W}(\tau_{\max})$ was introduced and it represents the temporal averaged value of the stored energy in a given time window:

$$\overline{W}(\tau_{\max}) = \frac{1}{\tau_{\max}} \int_0^{\tau_{\max}} d\tau \langle H_0 \rangle_\tau . \tag{4.22}$$

This quantity characterizes fluctuations in the stored energy due to time-dependent changes in $H(t)$, reflecting the stability of energy storage over the charging duration.

Moreover, Rosa *et al.* [21] identify the *disorder fluctuations*, related to an indetermination in the stored energy due to an inevitable fabrication imperfections in the battery, and *quantum fluctuations* associated with the fact that the evolved state $|\psi(t)\rangle$ is generally not a an eigenstate of H_0 i.e it is superposition of its eigenstates.

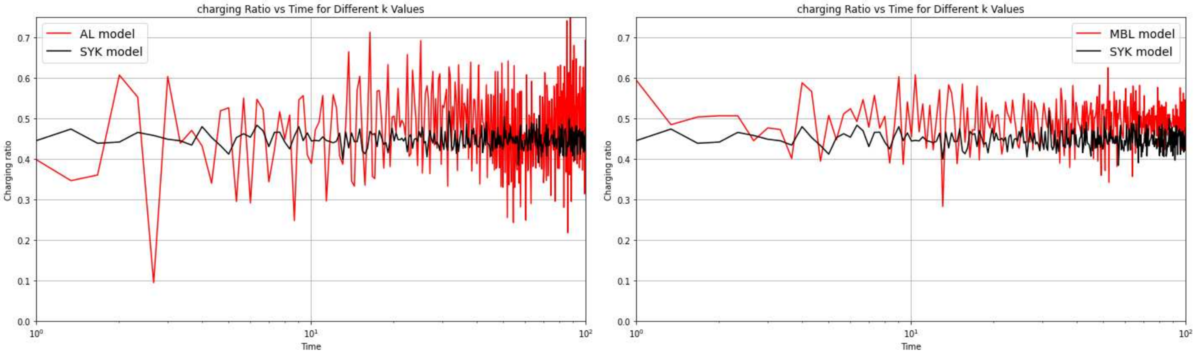

(a) AL model (b) MBL model

Figure 4.8: The sored energy normalized with respect to the bandwidth for the SYK model in black and in red the Al model for the figure (a) and the MBL model for the figure (b).

The two fluctuations can be defined as follow:

$$\left[\sigma_N^{(d)}(\tau)\right]^2 \equiv \langle\langle \langle H_0^2 \rangle_\tau \rangle\rangle - \langle\langle \langle H_0 \rangle_\tau \rangle\rangle^2 , \tag{4.23}$$

$$\left[\sigma_N^{(q)}(\tau)\right]^2 \equiv \langle\langle \langle H_0^2 \rangle_\tau - \langle H_0 \rangle_\tau^2 \rangle\rangle . \tag{4.24}$$

An optimal battery should achieve high stored energy while keeping fluctuations to a minimum and, in order to analyze the relative importance of those, we define the normalized quantities:

$$\Sigma_N^{(t,d,q)}(\tau) \equiv \frac{\sigma_N^{(t,d,q)}(\tau)}{\omega_{H_0}}, \tag{4.25}$$

where ω_{H_0} is the bandwidth defined in chapter 2.1.

In this chapter, not only the SYK model will be considered, but also other models that will allow a comparative analysis of the properties. The other Hamiltonian are based on the following:

$$\mathcal{H}_1 = -\sum_{j=1}^{N} J_j \sigma_j^x \sigma_{j+1}^x + J_2 \sum_{j=1}^{N} \sigma_j^x \sigma_{j+2}^x . \tag{4.26}$$

Here the first term describes a nearest-neighbor spin-spin interactions, while the second one next-to-nearest-neighbor interactions. The first couplings $J_j = J + \delta_j$ are the compositions of a constant part J and a contribution δ_j which varies randomly, for every index j on a uniform distribution $\delta_j \in [-\delta J, \delta J]$. The Hamiltonian 4.26 can exhibit a variety of different quantum phases, each of these associated with different values of the couplings.

In the following we will focus on the Many-body localization (MBL) phase with $J_2 = 0.3$ and $\delta J = 5$ and on the Anderson localization (AL) phase with $J_2 = 0$ and $\delta J = 1$. In the last part of the chapter it will be useful also the ergodic phase with $J_2 = 0.3$ and $\delta J = 1$. These values are taken from the work by Rossini *et al.* (2019) [22].

Finally, we note that Rosa *et al.* [21] used a real (Majorana) SYK model, whereas our study uses the complex SYK (c-SYK) model, which introduces additional structure in the charging dynamics.

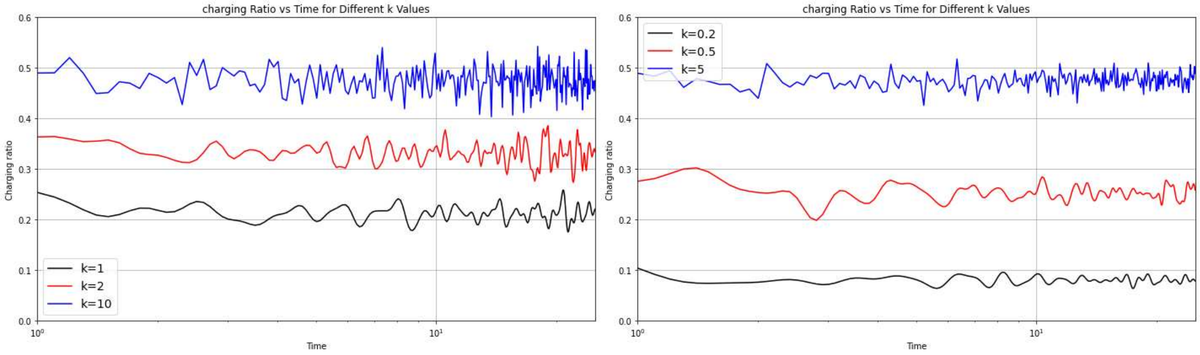

(a) AL model (b) MBL model

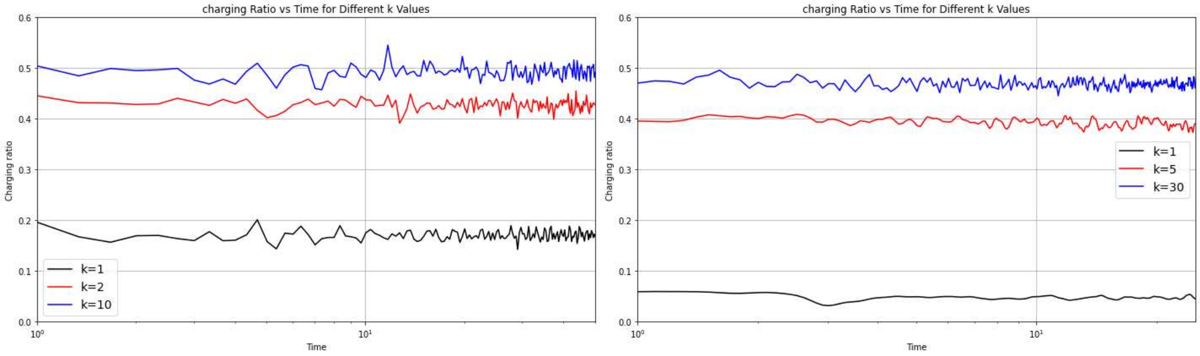

(c) ergodic model (d) SYK model

Figure 4.9: Charging ratio R as a function of time for AL, MBL, ergodic and SYK (more precisely complex SYK model) for different values of k. These curves are related to 15 realizations of the different models.

4.6.1 Charging ratio

A first quantitative result is obtained by defining the so-called charging ratio:

$$R(t) = \frac{W(t)}{\omega_{H_0}} \tag{4.27}$$

where $W(t)$ is the stored energy at time t and ω_{H_0} is the bandwidth of the Hamiltonian H_0. It is important to notice that in the literature, the bandwidth ω_{H_0} is often written as $\omega_{H_0} = Nh$ where h refers to the contribution of the individual components of the quantum battery Hamiltonian; in our specific case $h = \omega_0 \sigma^y$. However, we adopt the more general definition provided in equation 2.2. The time evolution of the charging ratio for different model is shown in figure 4.9.

We observe a clear trend: the average value of the charge ratio $R(t)$ increases as the dimensionless parameter k increases reaching a maximum value of 1/2. This is interpreted by Rosa *et al.* [21] as a signature of a transition induced by the quench Hamiltonian. Specifically, when k becomes sufficiently large, the system evolves from the initial state $|0\rangle$ into a superposition of multiple eigenstates of H_0. These eigenstates are distributed symmetrically around the center of the energy spectrum (or bandwidth) of H_0, Consequently, the average energy $\bar{W}$ is approximately half of the total energy range of H_0, i.e., $\bar{W} \sim \omega_{H_0}/2$.

Additionally, it is important to highlight the differences in the magnitude of fluctuations across different models. In the figure 4.9 we observe that the fluctuations diminish as the degree of non-locality in the models increases. This observation suggests, as mentioned in chapter 4.5 and illustrated in figure 4.2, that the non-locality and the all-to-all nature of the interactions of the SYK model are crucial for the quantum batteries performance.

Figure 4.8a and 4.8b provide a direct comparison between the SYK model, the Anderson localized (AL) model, and the many-body localized (MBL) model. These results, obtained from a single realization of the respective Hamiltonians, further emphasize the impact of non-local interactions on the stability and efficiency of quantum batteries.

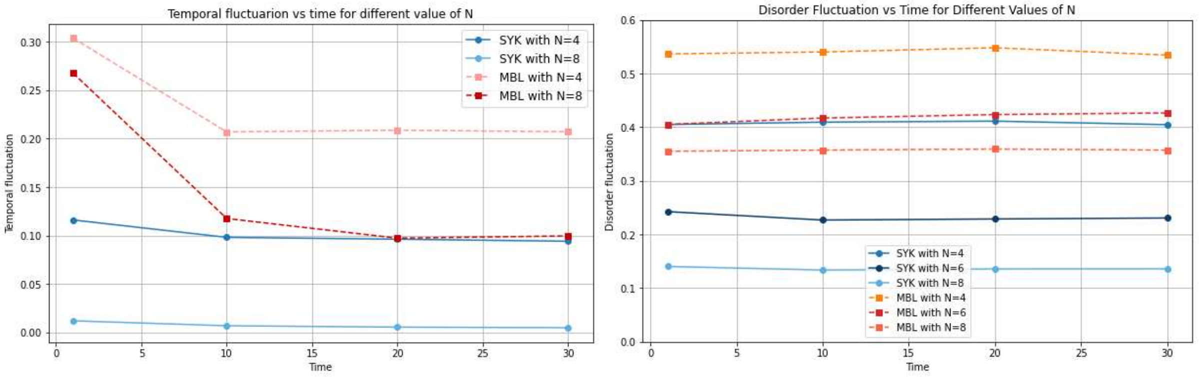

(a) Temporal Fluctuations

(b) Disorder Fluctuations

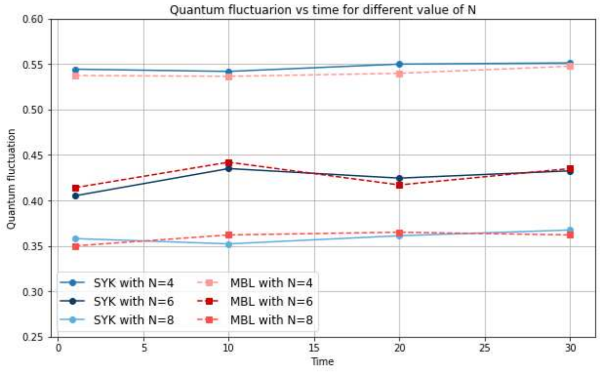

(c) Quantum Fluctuations

Figure 4.10: Temporal fluctuation for the SYK and AL model as a function of time for different values of N (a); disorder fluctuations for the SYK and MBL model as a function of time for different values of N (b); quantum fluctuations for the SYK and MBL model as a function of time for different values of N (c).

4.6.2 Fluctuations

We can go further and try to explicitly study an estimate of the relative importance of the different types of fluctuations. First we analyze the disorder and the quantum fluctuations by plotting the quantities $\Sigma_N^{(d,q)}(\tau)$ as a functions of the time for different values of N; the results are presented in the figure 4.10.b and 4.10.c.

The disorder fluctuations in the SYK model are significantly smaller when compared to the fluctuations observed in the MBL model for the same system size N. In particular, the SYK model exhibits notably reduced disorder-induced variability, highlighting its greater stability relative to the MBL model under similar conditions.

In the case of quantum fluctuations, unlike the disorder case, the fluctuations in both the SYK and MBL models are comparable. Moreover the intensity of the instability is way bigger than the other models. Rosa *et al.* [21] suggest that the relatively high level of quantum fluctuations observed in the SYK model may be linked to its notably high charging power. Indeed, recent studies indicate that large quantum fluctuations are essential for enhancing the charging power of quantum batteries. This correlation provides a plausible explanation for the high performance of the SYK model in this context.

The final case under consideration is that of temporal fluctuations, as illustrated in Figure4.10.a. The plot reveals a rapid decrease in fluctuations at early times, followed by a more gradual decline that approaches near stability. This suggests that, after an initial transient phase, the system reaches a regime where temporal fluctuations become significantly reduced, stabilizing over time.

Furthermore, all of the fluctuations follow a similar trend—namely, a suppression associated with increasing the size of the battery. In Rosa *et al.* [21], this analysis was carried out for temporal fluctuations over a broader range of N values, showing that the numerical data for the SYK case can be well described by the function:

$$\Sigma_N^{(t)} = aN^{2.5}2^{-N} + b, \tag{4.28}$$

whereas the MBL case can be described by the following:

$$\Sigma_N^{(t)} = \frac{a}{\sqrt{N}} + b, \quad \Sigma_N^{(t)} = aN^2 2^{-N} + b, \tag{4.29}$$

with the first expression applying at early times and the second at later times. Here a and b are fitting parameters. Thus, in the SYK model, temporal fluctuations are exponentially suppressed as the size of the battery increases; on the other hand, in the MBL model, fluctuations are suppressed primarily at late times, suggesting different mechanisms governing the dynamics of these two systems.

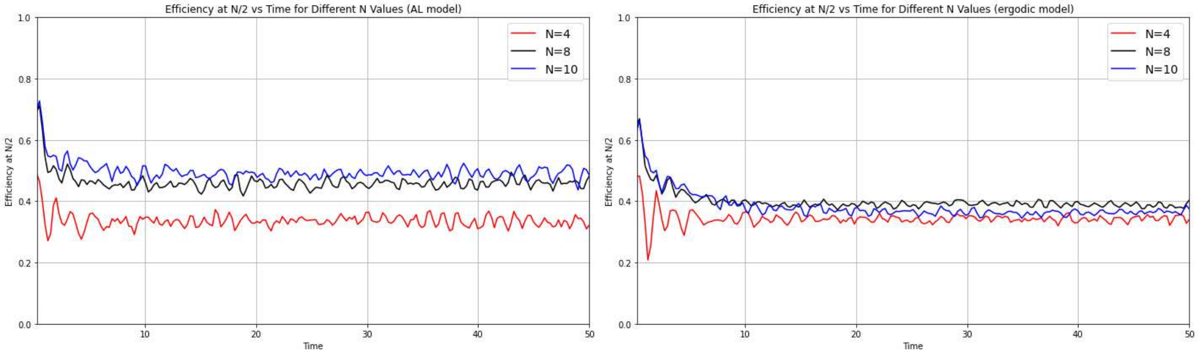

(a) AL phase (b) Ergodic phase

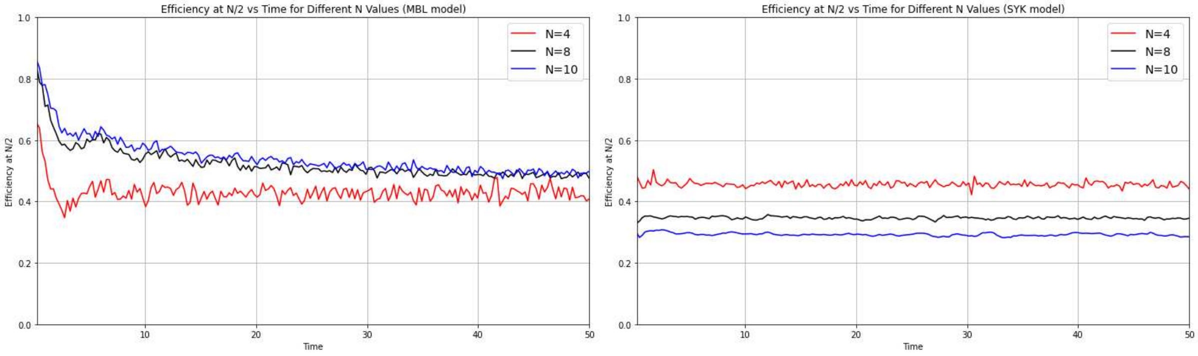

(c) MBL model (d) SYK model

Figure 4.11: $\langle\langle \mathcal{E}_{N/2}(\tau)/E_{N/2}(\tau)\rangle\rangle$ as a function of the time for different value of N. Shape for the AL phase in figure (a), shape of the ergodic phase in (b) and finally the shape for the SYK model in figure (c).

4.6.3 Efficiency

We can now analyze the relationship between the energy stored in the battery and the fraction of this energy that can be extracted (i.e the ergotropy), which determines the efficiency of the quantum battery. To quantify this, we define the disorder-averaged fraction of useful energy in half of the battery as a function of time:

$$\left\langle\left\langle \frac{\mathcal{E}_{N/2}(t)}{W_{N/2}(t)} \right\rangle\right\rangle, \tag{4.30}$$

where $\mathcal{E}_{N/2}(t)$ and $W_{N/2}(t)$ are the ergotropy and the energy at time t in half of the system. The results are presented in the figure 4.11. Figures 4.11.a and 4.11.b display this ratio for the Anderson localized and many-body localized model for different value of N. These results are consistent with the following asymptotic behavior:

$$\lim_{N\to\infty} \langle\langle \mathcal{E}_{N/2}(t)/W_{N/2}(t)\rangle\rangle = 1. \tag{4.31}$$

In both models, the ratio approaches unity in the thermodynamic limit, indicating that in large systems, nearly all the stored energy becomes extractable as ergotropy.

Although the AL and MBL phases exhibit the same asymptotic behavior, the underlying mechanisms are different. For the AL phase, only a small portion of the entire Hilbert space is explored during the system's dynamics. As a result, the difference between stored energy and ergotropy vanishes in the thermodynamic limit, as fewer states are occupied, and the battery becomes more efficient. In the case of the MBL phase, on the other hand, the system is dynamically frozen do to an extensive number of localized constants of motion. These constants of motion restrict the system's ability to explore the Hilbert space, and as a consequence, and the bipartite entanglement entropy follws an area-law scaling. This localized behavior also leads to the stored energy becoming almost entirely extractable as ergotropy in the thermodynamic limit, despite the system's highly constrained dynamics.

A different scenario is illustrated in figure 4.11.b, which presents the ratio described in equation 4.30 for the ergodic phase. In this case, he ratio appears to saturate at a finite constant as the thermodynamic limit is approached. This behavior is consistent with the fact that in the ergodic phase, the system explores the entire Hilbert space during its dynamical evolution, and the evolved state locally resembles a canonical ensemble.

Finally we can analyze the case of the SYK model, illustrated in figure 4.11.d. In this case, the efficiency of the battery, when considering half of the system, decreases as the number of particles N (i.e. the size of the battery) increases. This suggests that the fraction of extractable energy from the battery diminishes as the thermodynamic limit is approached.

This observation aligns with a similar result reported by Rosa et al. [21]. where the authors employed a different diagnostic. In particular, they examined the fraction of energy, per cell, that could be extracted from a reduced battery composed of M cells, out of an initial N cells. This can be quantify in the equation:

$$X_{M,N}(\tau) \equiv \left\langle\left\langle \frac{\mathcal{E}_M^{(N)}(\tau)/M}{W_N(\tau)/N} \right\rangle\right\rangle, \tag{4.32}$$

Their findings indicated that it is not advantageous to construct large batteries using the SYK protocol and then extract energy from only a portion of the battery at the end of the charging process.Instead, they concluded that it is more efficient to directly work with smaller batteries.

4.7 Sparse SYK quantum batteries

In this chapter, we extend the discussion of sparsity and its relationship with quantum chaos, as introduced in Chapter 3.6, to the context of the Sachdev-Ye-Kitaev (SYK) quantum battery. In particular we studied the behavior of the charging ratio $R(t)$ and the efficiency $\mathcal{E}(t)/W(t)$ as a function of the sparsity parameter p at fixed time. Moreover we also explore the relative importance of quantum, disorder, and temporal fluctuations as sparsity varies. These are done for the number of interacting particles N equal to 6 and 8.

4.7.1 Charging ratio and efficiency

The results for the charging ratio and efficiency are presented in table 4.12a for $N = 6$ and in figure 4.12b for N=8. The figure shows that both the charging ratio and the efficiency increase as the sparsity parameter p decreases form 1 to a threshold near the red-dotted line which represents the $p = p_2$ value defined on the chapter 3.6. Subsequently, for $p < p_2$, a pronounced decline in these metrics is observed.

At high p values, where the dynamics are less sparse, the system preserve a larger number of interaction terms. This increased connectivity can enhance the system's ability to store energy and make it easily available when needed, as reflected in the initial improvements in both R and efficiency. For moderate sparsification (slightly reducing p) the number of interaction terms are reduced, slightly simplifying the system without completely breaking its chaos. This reduction in complexity may allow the SYK battery to function more efficiently, leading to the observed increase show in the figure for intermediate sparsity.

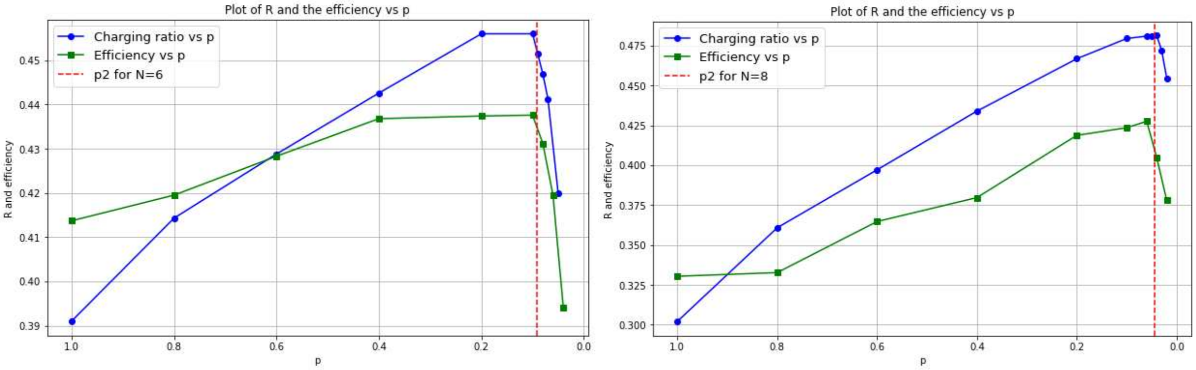

(a) SYK model with N=6

(b) SYK model for N=8

Figure 4.12: The charging ratio and the efficiency as a function of the sparsity parameter p for $N = 6$ (a) and $N = 8$ (b). The vertical red dotted line represents the value of the transition point p_2.

However, as p approaches the threshold p_2, the SYK model transitions into a regime where spectral rigidity and quantum chaotic properties significantly weaken. Therefore the model's eigenvalue statistics deviate strongly from RMT predictions, indicates a deterioration in the system's ability to scramble information effectively, a crucial property for high-performance quantum batteries. This loss of chaos is directly linked to the observed sharp declines in both R and efficiency.

These results suggest the existence of a optimal range of sparsity, slightly above p_2, where the balance between maintaining quantum chaos and reducing interaction complexity is ideal for maximizing the performance of SYK quantum batteries. Moreover, the diminishment of charging ratio and efficiency with increasing size of the battery is still visible.

We note that if we increase the strength of the interaction the charging ratio R and efficiency behave in a similar way to what is presented in the table 4.4; as the interaction becomes more strong the values increase up to the maximum values show the figures 4.12a and 4.12b, to then decrease after reaching the transition point p_2.

4.7.2 Fluctuations

We now move to analyze the magnitude of the different type of fluctuations presented in chapter 4.6.2. The results are shown in table 4.2 and table 4.3 in which we presente the fluctuation for different values of the sparsity parameter p, couplings strength and battery size N.

p	N=6		N=8	
	Quantum Fluc.	Disorder Fluc.	Quantum Fluc.	Disorder Fluc.
Low Coupling				
1	0.2353	0.2446	0.1420	0.1378
0.6	0.3269	0.3371	0.2061	0.2115
0.3	0.3965	0.4074	0.3083	0.3048
0.1	0.4096	0.4149	0.3832	0.3927
High Coupling				
1	0.4146	0.4158	0.3815	0.3840
0.6	0.4107	0.4135	0.3752	0.3670
0.3	0.4164	0.4031	0.3552	0.3594
0.1	0.4251	0.43369	0.3613	0.3575

Table 4.2: Comparative analysis of quantum and disorder fluctuations for N=6 and N=8 across different sparsity levels p, segregated into low and high coupling data sections. or low coupling we assume that the maximum value of the coupling J is 2, while for high coupling $J = 10$.

For the quantum fluctuations we observed that at low coupling strengths they increase as p decreases. This trend suggests that reducing the number of interaction terms amplifies the influence of the remaining terms, thus increasing quantum uncertainty. At high coupling strengths, however, the response to sparsity varies with system size.

For $N = 6$ quantum fluctuations exhibit stability across varying levels of sparsity, suggesting robustness in the quantum battery system of this size to maintain coherence and operational efficiency regardless of interaction density variations.

For $N = 8$, on the other hand, slight reduction in quantum fluctuations is observed as p decreases. This reduction might indicate that, as the system size increases, it becomes slightly more susceptible to the effects of sparsity, potentially leading to less quantum uncertainty in a more sparse configuration. This could imply that larger systems may better tune quantum effects under reduced interaction complexity. In the case of the disorder fluctuations the situation is equivalent.

These observations suggest that the response of quantum and disorder fluctuations to sparsity is not only dependent on the sparsity itself but also significantly influenced by the system size. Particularly, larger systems may show a gradual alignment of fluctuation behaviors, trending towards reduced variability and enhanced stability as interactions become sparser.

p	Temporal Fluctuations			
	Low Coupling		High Coupling	
	N=6	N=8	N=6	N=8
1	0.0377	0.0122	0.2297	0.2246
0.6	0.0733	0.0282	0.2113	0.1953
0.3	0.1490	0.0633	0.1833	0.1655
0.1	0.2333	0.1650	0.1415	0.1342

Table 4.3: Temporal fluctuations for $N = 6$ and $N = 8$ across different sparsity levels p, segregated into low and high coupling data sections.

In the case of the temporal fluctuations the situation in different. At low coupling strength, they behave similarly to quantum and disorder fluctuations. However, at high coupling strength, temporal fluctuations consistently decrease as sparsity increases, suggesting improvements in the system's temporal coherence with fewer interactions. This decline in fluctuation magnitude suggests an improvement in the system's temporal coherence as the number of interactions increases.

This analysis of quantum, disorder, and temporal fluctuations within the SYK quantum battery show distinct behaviors at low and high coupling strengths, underling their influence on system performance.

At low coupling, the increase in fluctuations with greater sparsity; this increased sensitivity can amplify quantum chaos and disorder, potentially enhancing the dynamical capabilities of the system, but at the cost of reducing predictability and stability.

In contrast, high coupling strengths show a consistent decrease in fluctuations with increasing sparsity. This trend suggests that the system prioritizes stability as it becomes sparser.

These results suggest the need of carefully balance system parameters to manage the trade-offs between enhancing quantum capabilities and maintaining operational stability.

4.8 Disorder-free SYK quantum battery

In this section we analyze a quantum battery based on the model studied by Ozaki *et al.* [20], that is a disorder-free SYK model. This is defined, with uniform couplings, as:

$$H_4 = i^2 \sum_{1\le i_1<i_2<i_3<i_4\le N} \gamma_{i_1}\gamma_{i_2}\gamma_{i_3}\gamma_{i_4}, \tag{4.33}$$

where γ_i $(i = 1, \dots, N)$ are Majorana fermions satisfying $\gamma_i^\dagger = \gamma_i$ and $\{\gamma_{i_1}, \gamma_{i_2}\} = 2\delta_{i_1,i_2}$.

It is possible to analytically diagonalize the quartic Hamiltonian H_4 by introducing the auxiliary quadratic Hamiltonian:

$$H_2 = i \sum_{1\le i_1<i_2\le N} \gamma_{i_1}\gamma_{i_2}. \tag{4.34}$$

The Hamiltonians H_2 amd H_4 are related by the relation:

$$H_4 = \frac{1}{2}(H_2)^2 + E_0, \tag{4.35}$$

where E_0 and the square of H_2 can be written as:

$$E_0 = -N(N-1)/4, \quad (H_2)^2 = i^2 \sum_{i<j} \sum_{k<l} \gamma_i \gamma_j \gamma_k \gamma_l. \tag{4.36}$$

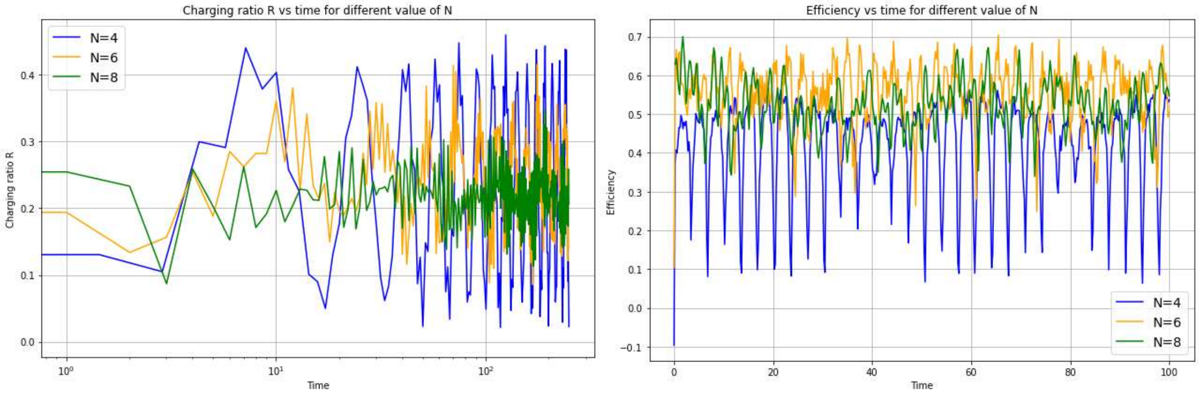

(a) Charging ratio

(b) Efficiency

Figure 4.13: (a) shows the charging ratio R as a function of time while (b) shows the efficiency at half of the battery in terms of the time. Both the plot display the results for different values oh N.

The authors found that this models exhibits exponential behaviors in OTOCs at early times, akin to those observed in certain quantum chaotic systems, which can be interpreted as a precursor of chaos. Moreover, unlike typical chaotic systems that involve disorder or external kick terms, the new model does not incorporate such elements.

	$k=5$	$k=15$	$k=30$	$k=50$	$k=1\cdot10^3$
N=4	0.2350	0.3156	0.4049	0.4479	0.4995
N=6	0.2409	0.2643	0.3176	0.3591	0.5020
N=8	0.2178	0.2876	0.3196	0.3361	0.4886

Table 4.4: Value of charging ratio for different N presented as for different values of the parameter k.

The analysis of the quantum battery is conducted using the charging protocol presented in Equation 4.20, which allows us to investigate the impact of varying interaction strengths. Figure 4.13a and 4.13b show the charging ratio R and the efficiency as a function of time for different value on N. From figure 4.13a it becomes evident that, as the number of qubits N increases, the charging ratio R exhibits greater stability, though its average value remains substantially unchanged. This observation is corroborated form the table 4.5, where a general decreasing of the fluctuations is highlighted.

Furthermore, table 4.4 shows how the charging ratio varies with the increase of the dimensionless parametr k. Initially, R stars as relatively low for $k=5$ and subsequently increases until the value of 1/2 where it converges. However, further increases in the interaction strength lead to a rapid escalation in fluctuations as presented in table 4.5.

These results suggest that, within the disorder free SYK model, a relatively big quantum battery is preferable to a smaller one. A large N provides better stability in the charging ratio, indicating a more reliable charging process.

This conclusion is supported by figure 4.13b which shows the efficiency at half of the battery (i.e. the ratio $\mathcal{E}_{N/2}(t)/W_{N/2}(t)$) over time for different values of N. Differently from figure 4.11, where the ratio decreases as the size N increases, we observed distinct behavior for the disorder-free SYK Hamiltonian: the efficiency increases with N and it appears to converge toward a value close to 1/2. This suggests that, within this model, larger quantum batteries become progressively more efficient, reaching an asymptotic limit as N grows.

Moreover, for larger values of N, the ratio $\mathcal{E}_{N/2}(t)/W_{N/2}(t)$ shows significantly reduced fluctuations, leading to much more stable performance over time. This stability is advantageous, because suggests that larger quantum batteries not only achieve higher efficiency, but also maintain it consistently.

k=5	N=4	N=6	N=8	k=15	N=4	N=6	N=8
Disorder F.	0.6704	0.5569	0.5804	Disorder F.	0.8801	0.6850	0.6316
Quantum F.	0.6704	0.5569	0.5804	Quantum F.	0.8801	0.6850	0.6316
Temporal F.	0.2523	0.1349	0.0812	Temporal F.	0.3114	0.1890	0.1318

Table 4.5: The different type of fluctuations for different values of N and different value of k.

The presented results suggest that, to optimize the performance of a disorder-free SYK quantum battery, one should consider utilizing a large battery and potentially a selected value of the interaction parameter k, aiming to achieve a charging ratio close to 1/2. However, it is crucial to choose an appropriate value of k that balances a high charging ratio with manageable fluctuation levels. Thus, an optimal configuration would involve maximizing R while keeping fluctuations within an acceptable range.

Chapter 5

Conclusions

In this thesis we analyzed important concept of Quantum Battery, particularly a version of it based of the Sachdev-Ye-Kitaev model.

We described the fundamental aspects of the quantum batteries beginning form the Hamiltonian construction. We focused on the different types of charging approach, namely the *parallel* and *collective* methods, and than introduced the *quantum advantage* which is the deep reason for the growing interest in this topic. Another fundamental concept exhibited in the work is the *ergotropy* that is the maximal amount of work that can be extracted from a state via *unitary operation*. In the first part of the thesis we also introduced the quantum speed limit (QSL) problem, a general bound on the minimum time required by a system to evolve from one state to another. We used the QSL to derive useful theoretical bounds we utilized to test the validity of our models.

Moving to a more specific focus, we explored the Sachdev-Ye-Kitaev model,which is a fundamental part of this work, and we introduced it in the second part of the thesis. We highlighted the model's all-to-all interaction structure and quenched disorder properties. In addition to describing the two and four point functions (derived with the diagrammatic approach) we mentioned the Eigenstate Thermalization Hypothesis (ETH) and the self averaging nature of the SYK properties. We introduced a fundamental variation of the Sachdev-Ye-Kitaev model, the so called sparse model. This in crucial since it significantly reduced the number of the interaction terms and, consequently, the computational resources required for a simulation. Finally, we study how the "sparsification" influences the chaotic nature of the SYK model, focusing on the extraction of two transition points: p_1 and p_2. The point p_1 is defined as the largest value of the sparsity parameter p for which the SFF of the sparse model significantly deviates from the spectral form factor of the unsparsified model; the point p_2, on the other hand, denotes the value of p for which the nearest-neighbor gap ratio diverges from the predictions of Random Matrix Theory, marking a significant loss of spectral rigidity.

With this understanding of the SYK model and its variants, we moved to the final part of this thesis, where we investigated SYK quantum batteries. Our approach involved both a direct analysis and comparative evaluations with other models. We started our analysis with the introduction of the charging protocol and with some preliminary considerations regarding the population dynamics and the charging power. Subsequently we discussed the used time evolution: the Lindblad master equation, which is an extension of the Liouville-von Neumann equation that allows for the inclusion of non-unitary processes, making it suitable for modeling open quantum systems. We introduced different models (many-body localization, Anderson localization and ergodic) which helped us to quantify the characteristics of the SYK model. We specifically examined the charging ratio for different value of the coupling strength and relative importance of temporal, quantum and disorder fluctuations. We also analyzed the efficiency at half of the battery for different size of the of it. In agreement with other papers we found, between the analyzed, the SYK quantum batteries are the more stable and their efficiency is maximized for small systems.

In the concluding sections we studied two different type of SYK quantum batteries. First we applied the transition point p_1 and p_2: the obtained results suggest the existence of a optimal range of sparsity, slightly above p_2, where the balance between maintaining quantum chaos and reducing interaction complexity is ideal for maximizing the performance of SYK quantum batteries. Moreover, the analysis of the fluctuations show distinct behaviors at low and high coupling strengths, suggesting the need of a "fine tuning" between p, coupling strength and battery dimension. Finally we studied the case of a disorder-free SYK quantum battery. Differently from the standard case, to optimize this battery one should consider utilizing a large battery and potentially a selected value of the interaction strength in order to balance a high charging ratio with manageable fluctuation levels.

Due to practical limitation, we limited our study the quantum batteries of small dimension, specifically $4 \leq N \leq 8$. To gain a more comprehensive understanding of the impact of spasrification on the performance of the quantum batteries, it would be valuable to extend the analysis to systems with a broader range of interacting particles, which includes larger values of N. For the same reason, increasing the size of the disorder-free quantum batteries could provide further insights into whether the observed trends in performance and stability persist in larger systems. On the other hand, also a more in-depth study on the influence of the adimensional parameter k could be considered.

5.1 Summary of SYK quantum batteries results

Standard SYK QB. The SYK quantum batteries is *the most stable* between the investigated cases. This is clear form the figures 4.8a, 4.8b and explicitly form chapter 4.6.2. In that section we analyzed the relative importance of the different types of fluctuations and we show that the *quantum-related instability is the most relevant*, enhancing the charging power of quantum batteries. Moreover, chapter 4.6.3 suggests that it is *more efficient to work with small batteries* (i.e. small number N), in agreement with [21].

Sparse SYK QB. In this section the results suggests the existence of a *optimal range of sparsity* where the balance between maintaining quantum chaos and reducing interaction complexity is ideal for maximize performance. This trend is clear from the figures 4.12a and 4.12b. Furthermore, in tables 4.2 and 4.3 we see that, in general, *fluctuations strength increases with the interactions importance and decreases with the size of the batteries.* Moreover, the diminishment of charging ratio and efficiency with increasing size of the battery is still visible.

Disorder-free SYK QB. In the disorder free case as the number of qubits N increases, *the stability of the system grows* as presented in figures 4.13a and 4.13b. Moreover the charging ratio in linearly correlated with the interaction strength. On the other hand, however, also *the fluctuations grows with k.* This shows that a *relatively big quantum battery is preferable* to a smaller one and that one have to choose an *appropriate value of k that balances a high charging ratio with manageable fluctuation levels.*

Overall the three types of quantum batteries share a common behavior with regards to the fluctuations in terms on the battery size N: they decrease as N grows. At the same time, in standard and sparse batteries there is a diminishment of efficiency and charging ratio with the growing of N but in disorder free batteries they remain nearly unchanged.

Appendix A

Appendix

A.1 More on the Liouville-von Nuemann equation

As we said in chapter 2.1, the Liouville-von Neumann equation describes the time evolution of the density matrix in a closed quantum system. It is a quantum analogue of the classical Liouville equation and it can be written as:

$$\frac{d\rho}{dt} = -\frac{i}{\hbar}[H, \rho] \tag{A.1}$$

where ρ is the density matrix representing the system's state and H is the Hamiltonian that generates the unitary evolution.

The Liouville-von Nuemann equation is related to the unitary evolution for the density matrix. To see this connection, let us consider an initial state $\rho(0)$ and analyze its evolution under the action of H. In a closed system, the time evolution of any quantum state is governed by a unitary operator $U(t) = e^{-\frac{i}{\hbar}Ht}$ resulting in the evolved state:

$$\rho(t) = U(t)\rho(0)U^\dagger(t). \tag{A.2}$$

Now we can take the time derivative of the last expression:

$$\frac{d\rho(t)}{dt} = \frac{d}{dt}\left(U(t)\rho(0)U^\dagger(t)\right) = \frac{dU(t)}{dt}\rho(0)U^\dagger(t) + U(t)\rho(0)\frac{dU^\dagger(t)}{dt}, \tag{A.3}$$

Explicitly writing the derivative of the unitary operators as:

$$\frac{dU(t)}{dt} = -\frac{i}{\hbar}HU(t), \quad \frac{dU^\dagger(t)}{dt} = \frac{i}{\hbar}U^\dagger(t)H \tag{A.4}$$

we can rewrite the equation A.3 as:

$$\frac{d\rho(t)}{dt} = -\frac{i}{\hbar}HU(t)\rho(0)U^\dagger(t) + \frac{i}{\hbar}U(t)\rho(0)U^\dagger(t)H = -\frac{i}{\hbar}[H, \rho(t)]. \tag{A.5}$$

Thus, the Liouville-von Neumann equation formally expresses how the density matrix evolves unitarily in time when subjected to a Hamiltonian H, and the commutator $[H, \rho(t)]$ ensures that this evolution preserves the trace and positivity of $\rho(t)$. Moreover, the unitary nature of this evolution implies that coherence (the phase relationships between quantum states) is preserved over time, as no information is lost to the environment.

Furthermore the The Liouville-von Neumann equation acts as a generator of motion for the density matrix in operator space, analogous to the role of the Schrödinger equation for pure states in Hilbert space. In closed systems, it preserves probability and coherence, keeping the entropy of the density matrix constant. In open systems, on the other hand, there is as interaction with an environment that leads to decoherence and entropy increase. In order to account for the dissipation modifications are required (typically Lindblad operators).

A.2 More on chaos

In this appendix, we present a more precise description of the nature of chaotic systems, following the formalism described by Maldacena *et al.* [16].

Chaos, particularly in its strong form, is a crucial phenomena in physics of particular interest to quantum mechanics. A standard way to study this phenomenon is to consider the commutator $[W(t), V(0)]$ where W and V are general Hermitian operators, representing the observables of the system, separated by a time t. This commutator describes how an initial perturbation by V influences later measurements of W, and conversely, how the presence of W affects the system's sensitivity to earlier perturbations by V. To quantify this effect we can use the define:

$$C(t) = -\langle [W(t), V(0)]^2 \rangle \tag{A.6}$$

where the $\langle - \rangle$ indicates the thermal expectation value at temperature β^{-1}. In general, we assume $V(0)$ and $W(0)$ as simple Hermitian operators, often expressible as a sum of local terms.

In chaotic systems, we can define two different time scale: (1) the time at which $C(t)$ becomes significant is called "scrambling time" and it is denoted as t_s; (2) the time associated to the exponential decay for two point expectation values of the type $\langle V(0)V(t) \rangle$ that is called "dissipation time" t_d. In a strongly coupled system $t_d \sim \beta$.

Considering the semiclassical limit of a one particle quantum chaotic system we arrive to a quantitative interpretation of the relation between equation A.6 and chaos. In this limit, if we take $V = p$ and $W(t) = q(t)$, their commutator converges the Poisson bracket:

$$i\hbar\{q(t), p\} = i\hbar \frac{\partial q(t)}{\partial q(0)}, \tag{A.7}$$

reflecting the sensitivity of the final position to infinitesimal variations in the initial position. In this situation, nearby trajectories in phase space diverge exponentially, following $e^{\lambda_L t}$ where λ_L denotes the Lyapunov exponent. Consequently, we get:

$$C(t) \sim \hbar^2 e^{2\lambda_L t} \quad \text{so} \quad t_s \sim \frac{1}{\lambda_L} \log \frac{1}{\hbar}. \tag{A.8}$$

This exponential sensitivity to initial conditions is distinctive sign of quantum chaos and places a theoretical limit on how rapidly information can spread within a quantum system.

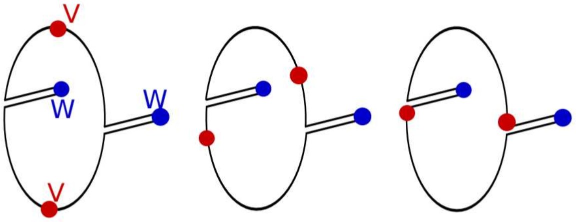

Figure A.1: Pictorial representation of the time-contour of the operators in the thermal circle, illustrating the correlation function $F(t)$ with operator insertions W and V. The circular arrangement represents imaginary time evolution, where $F(t+i\tau)$ corresponds to a rotation by an angle $2\pi\tau/\beta$ along the thermal circle. The folds in the contours indicate Lorentzian time evolution, yielding $W(t)$ as shown. In the left panel, we have $\tau = 0$ representing $F(t)$; the center panel corresponds to $|\tau| < \beta/4$, and the right panel to $\tau = \beta/4$. At late times t, as all pairs of operators become separated by large intervals, F decreases. This behavior is independent of τ, emphasizing the difference between contour ordering of correlation functions such as $VW(t)VW(t)$, which decay at large t, and $VWV(t)W(t)$, which do not. From Xu *et al.* [25]

Let us now consider the quantum mechanical point of view: we can use $C(t)$ as a measure of the growth of the operator $W(t)$. In general, if the interactions are local, the time for the commutator to build up is linearly proportional to the separation between W and V. However, if the interaction are non-local ,as is common in systems such as the SYK model, the scrambling time becomes $t_s \sim \log N$ for $C(t)$, where N is the total number of qubits in the system.

In quantum field theory the commutator A.6 is difficult to handle due to the need for regularization. Instead, it is often convenient to shift one of the commutator halfway around the thermal cycle in the imaginary time, and consider:

$$-\operatorname{tr}\left[y^2[W(t),V]y^2[W(t),V]\right] \quad \text{where} \quad y^4=\frac{1}{Z}e^{-\beta H}. \tag{A.9}$$

The latter equation can be written as follows:

$$\begin{aligned}-\operatorname{tr}\left[y^2[W(t),V]y^2[W(t),V]\right] &= \operatorname{tr}\left[y^2W(t)Vy^2VW(t)\right]+\operatorname{tr}\left[y^2VW(t)y^2W(t)V\right]\\ &\quad -F\left(t+i\frac{\beta}{4}\right)-F\left(t-i\frac{\beta}{4}\right).\end{aligned} \tag{A.10}$$

where we highlight the fact that $F\left(t-i\frac{\beta}{4}\right)=\operatorname{tr}\left[y^2VW(t)y^2VW(t)\right]$.

We can see that, for small t, all terms remain positive and comparable; therefore the commutator is small because of the cancellation between the first and the second lines. At large t, on the other hand, the traces in the first line remain of order one while the terms in the second line begin to decay. This behavior is the basis of the growth of the commutator, with the decay of F in late times being particularly significant.

To have more insight on the late time decrease of F, we can introduce the *thermofield double state* in the Hilbert state of two replicas of the quantum system:

$$|\mathrm{TFD}\rangle = Z^{-1/2}\sum_n e^{-\beta E_n/2}|\tilde{n}\rangle_L|n\rangle_R. \tag{A.11}$$

This is an entangled state and it has a very unique pattern of correlation between left (L) and right (R) components. In order to understand the behavior of the function F we consider the fact that $F(t)=\langle\Psi|V_LV_R|\Psi\rangle$ where:

$$|\Psi\rangle = Z^{-1/2}\sum_{m,n} e^{-\beta(E_m+E_n)/4}W(t)_{n\tilde{m}}|\tilde{m}\rangle_L|n\rangle_R. \tag{A.12}$$

For small t, the $W(t)$ operator produces only a minor perturbation, so the correlation between the two subsystems remains unchanged, keeping F large. As t increases, on the other hand, the W-induced perturbation will increases and the correlation will be destroyed, inducing the decreases of F. This behavior mirrors the concept of classical chaos, where initial correlations decay as trajectories diverge exponentially in phase space, highlighting the deep connection between quantum and classical chaos.

A.3 More on sparsification

The integration of expander graphs and hypergraphs as models for Hamiltonians broadens the potential for fast scrambling, underscoring the role of structural connectivity. Following Xu *et al.* [25], we will analyze this concept.

Consider an Hamiltonian which is a sum of terms acting on q vertices, commonly referred to as a q-local Hamiltonian.

For instance a 2-local system represents a discretization of a continuous space in which interactions occur between nearest neighbors, which are finite in number, and exhibit Heisenberg-type couplings.

Even in this context we can define the scrambling time t_s. However, the study of q-local systems expands our understanding of how this time scale depends on the underlying connectivity and interaction complexity within the system.

Scrambling is tied to the growth in complexity of initially simple Heisenberg operators. AS time increases, the operator, such as a single-site Pauli operator $\sigma^z(t)$, originally with support only on one vertex, gradually spreads across multiple vertices. Therefore as time progresses, the initially localized information about the type and the vertex associated to the operator, becomes impossible to recover with local measurements. This phenomenon, called information scrambling, reflects the loss of accessible information on the origin and nature of the initial operator and t_s represents the time required for the information to fully spread across all vertices.

We can now try to give an estimate of t_s. If S_t be the set of vertices with a specific information at time t, an estimation for a simple continuum model is:

$$\frac{d|S_t|}{dt} = \lambda|\partial S_t|, \tag{A.13}$$

where $|S_t|$ is the number of vertices with the information and $|\partial S_t|$ is the number of neighboring vertices. The information is completely scrambled when $|S_t| \sim N$ where N is the total number of vertices allowing us to estimate the scrambling time if we know the relation between $|S_t|$ and $|\partial S_t|$.

The use of lattice systems is not optimal due to their very sparse nature; in fact the number of edges grows linearly with N. In order to speed up the scrambling it could be useful to increase the number of terms in the Hamiltonian or the number of the interactions, but this consequently increase the cost of simulating the systems.

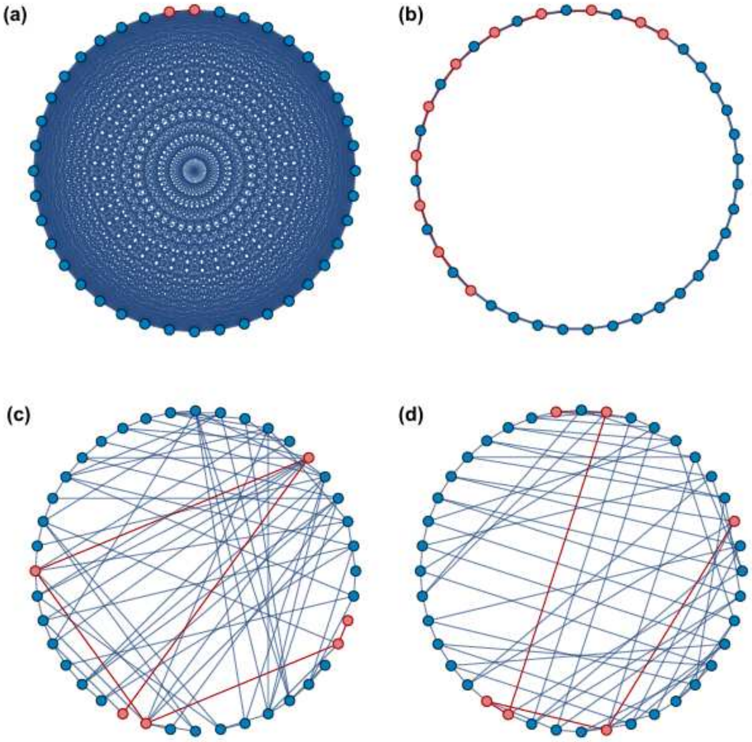

Figure A.2: Comparison between complete graph (a), one-dimensional lattice (b), random graph (c) and random regular graph (d). From Xu *et al.* [25]

.

A way to overcome this problem is to look for systems beyond lattice models. n particular, we will consider “sparse graphs” which have much stronger connectivity than lattices, thus emerging as promising alternatives for rapid scrambling. To be concrete, if we consider a subgraph S of an expander graph G, then it is true that:

$$|\partial S| \sim |S|, \quad \forall |S| < G/2. \tag{A.14}$$

If we insert this relation in equation A.13 we get again $t_s \sim \log N$. Consequently, expander graphs not only retain sparsity but also efficiently distribute information, qualifying them as fast scramblers.

At this point it is important to highlight the fact that expanders graphs represent a broad class, which includes random regular graphs (random graphs with fixed vertex degree d). Moreover, sparse random graphs, formed by randomly omitting vertices with a probability $p = 2k/N$, also function as expanders, generalizing the concept of scrambling beyond lattice systems.

Before concluding we introduce the q-local Hamiltonian with $q > 2$, corresponding to hypergraphs. These are particularly relevant because the 2-local fermionic systems are non-interacting and they do not scramble in the many-body Hilbert space. The interaction graph is constructed by including an edge between two vertices if and only if H contains an interaction term that includes both degrees of freedom. These connections represents nearest neighbors connections implying the Hamiltonian to be nearest neighbor coupled on the graph. Moreover if the graph is an expander than the Hamiltonian can exhibits fast scrambling.

A.4 More on Random Matrix theory

Random Matrix Theory (RMT) provides a powerful statistical framework for studying the distribution of eigenvalues in complex systems. Originally developed in nuclear physics to model the spectra of heavy nuclei, RMT has since found applications in various fields such as quantum chaos, condensed matter physics, and number theory.

RMT is built around the study of matrix ensembles with randomly distributed elements. The most common ensembles include the Gaussian Orthogonal Ensemble (GOE), Gaussian Unitary Ensemble (GUE), and Gaussian Symplectic Ensemble (GSE), each distinguished by specific symmetry properties. For instance, the GOE corresponds to systems with time-reversal symmetry, while the GUE applies to systems without time-reversal symmetry. These ensembles are characterized by their joint probability distributions and the correlations between eigenvalues.

One important feature of RMT is the Wigner semicircle law,which describes the eigenvalue density for large random matrices and highlights the universal nature of spectral distributions. For exemple ([19] and [12]), let us consider a single Gaussian random matrix H of size N with distribution proportional to $\exp(-\frac{1}{2}\mathrm{Tr}H^2)$. The eigenvalues $\lambda_1 \leq \cdots \leq \lambda_N$ show a density describes by the Wigner semicircle law:

$$\rho(\lambda) = \frac{1}{\pi\sqrt{2N}}\sqrt{2N-\lambda^2}. \tag{A.15}$$

The mean level spacing in the vicinity of $\lambda = 0$ is $\Delta = \pi\ \sqrt{2N}$ and this implies a local density of $1/\Delta = \sqrt{2N}/\pi$. In a region of constant density it is possible to write the nearest-neighbour spacing distribution. For a 2×2 matrices we have:

$$p(s) = a_\beta s^\beta e^{-b_\beta s^2}, \tag{A.16}$$

where a_β and b_β are normalization constant, chosen in such a way that $\langle s\rangle = 1$. in the case of a 3×3 matrices the nearest-neighbour spacing distribution can be written as:

$$p(s,t) = A_\beta s^\beta t^\beta (s+t)^\beta e^{-B_\beta(s^2+st+t^2)}, \tag{A.17}$$

where B_β is construct in such a way that $\langle s\rangle = \langle t\rangle = 1$ and A_β is an overall normalization factor.

Concretely, we can consider Gaussian unitary ensemble (GUE); in this case it is possible to define the normalized eigenvalue density (and the average density in this ensemble follows):

$$\rho(\lambda) = \frac{1}{N}\sum_i^N \delta(\lambda-\lambda_i) \to \langle\rho(\lambda)\rangle = \rho_{\mathrm{sc}}(\lambda) = \frac{1}{2\pi}\sqrt{4-\lambda^2} \tag{A.18}$$

With this normalization, the correlation among the eigenvalues can be expressed by the pair correlation function $R(\lambda_1, \lambda_2)$ and, when the average between the two eigenvalues $\bar{\lambda}$ is not close to the difference between the two, it can be written with the sine kernel formula as:

$$R(\lambda_1,\lambda_2) = \frac{\rho_{sc}(\lambda_1)}{\pi L}\delta(\lambda_1-\lambda_2) + \rho_{sc}(\lambda_1)\rho_{sc}(\lambda_2)\left(1 - \frac{\sin^2 x}{x^2}\right); \tag{A.19}$$

where $x \equiv \pi N\delta(\lambda_1-\lambda_2)\rho(\bar{\lambda})$.

Another crucial aspect of RMT is the study of level spacing distributions and nearest-neighbor gap statistics, which provide insight into whether a system exhibits regular or chaotic behavior. These statistical measures are crucial for the analysis of spectral rigidity, a concept that reflects the way in which eigenvalues resist deviations from their mean distribution.

Spectral rigidity is a measure of the extent to which eigenvalues of a system resist fluctuations from their average distribution, reflecting the system's degree of regularity or chaoticity. In the context of

RMT, spectral rigidity is closely related to the concept of level repulsion, which is a characteristic phenomenon of chaotic systems. The nearest-neighbor gap ratio defined as:

$$r = \left\langle \min\left(\frac{s_i}{s_{i+1}}, \frac{s_{i+1}}{s_i}\right)\right\rangle_i = \left\langle \min\left(\frac{E_i - E_{i-1}}{E_{i+1} - E_i}, \frac{E_{i+1} - E_i}{E_i - E_{i-1}}\right)\right\rangle_i , \tag{A.20}$$

on the other hand, serves as a practical tool for assessing spectral rigidity. The gap ratio has the advantage of being scale-invariant, meaning it does not require unfolding of the spectrum and can be directly used to probe universal spectral properties. In chaotic quantum systems, the average gap ratio follows a characteristic value that aligns with predictions from the Gaussian ensembles (e.g., for GOE and for GUE).

	m	GOE	GUE	GSE
$\langle r\rangle$	1	0.5307(1)	0.5996(1)	0.6744(1)
$\langle r\rangle_m$	2	0.4235(5)	0.4220(5)	0.4116(5)
	3	0.4035(5)	0.3992(5)	0.3927(5)
	4	0.3963(5)	0.3924(5)	0.3886(5)

Table A.1: Average nearest-neighbor gap ratios for different Gaussian ensembles (GOE, GUE, GSE) for various m values. Taken form Giroud *et al.* [12].

To illustrate these properties more concretely, we consider ensembles of random matrices of size N which can be decomposed into m independent blocks of sizes $N_1, N_2, \ldots, N_m$. From this consideration Giroud *et al.* found the value of the average gap ratio for the GOE, GUE and GSE for different values of m, and they are presented in table A.1.

A.5 Hopping operator

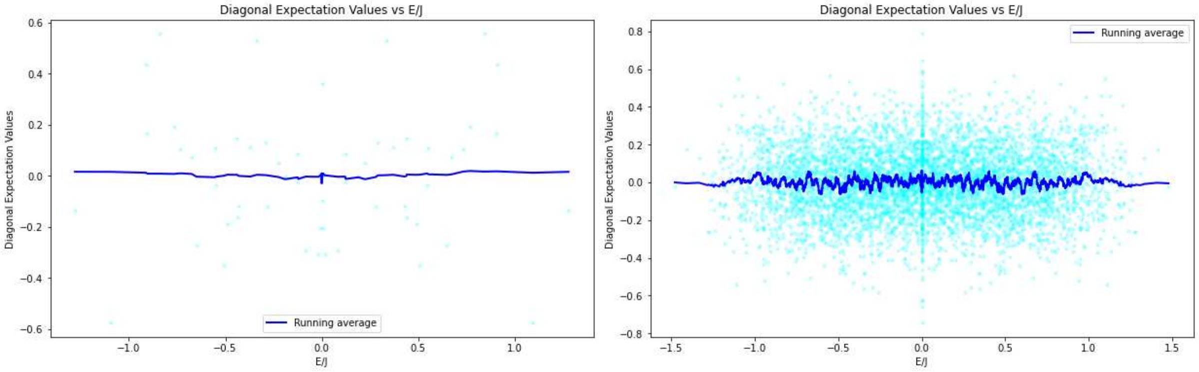

(a) 1 repetition

(b) 100 repetitions

Figure A.3: Diagonal expectation values for the two-site hopping operator $h_{N-1,N}$at half filling $\upsilon = 1/2$. (a) shows the results for one representation and (b) shows the same after an average over one hundred realizations. We see that the two show the same behavior, indicating that the operaotr is self averaging.

The discussion presented in Chapter 3.1.2 regarding the thermalization process is expected to apply to any non-extensive operator within the SYK model. To demonstrate that this holds true beyond the specific example of the on-site number operator, we present here the analysis for an operator that differs significantly: the two-site hopping operator.

This is a Hermitian operator written as:

$$h_{ij} = c_i^\dagger c_j + c_j^\dagger c_i \tag{A.21}$$

where c_i^{dagger} and c_i are the fermionic creation and annihilation operators, respectively. The indices i and j represent two arbitrary chosen sites within the system. Importantly, the hopping operator conserves the total fermion number, which highlights its suitability for studying thermalization in a system that respects the conservation of the number of particles.

The results are shown in figures A.3a and A.3b. As before,we differentiate between the outcomes obtained from a single, randomly chosen realization of the SYK Hamiltonian (shown in the left panel) and the averaged results over 100 independent realizations (displayed in the right panel). We recall that the single realization offers insight into the behavior of the system under individual random conditions, while the ensemble average reveals the extent to which the system exhibits self-averaging properties.

The findings clearly indicate that, in both cases, there is convergence towards a limiting curve; this behavior confirms that the operator undergoes thermalization, aligning with the broader conclusions about non-extensive operators within the SYK framework. The averaging over multiple realizations further emphasizes the robustness of the thermalization process and suggests that self-averaging is a fundamental characteristic of the model.

Bibliography

[1] Kitaev Alexei. A simple model of quantum holography(part 2), 2015.

[2] Kitaev Alexei. A simple model of quantum holography(part1), 2015.

[3] Robert Alicki and Mark Fannes. Entanglement boost for extractable work from ensembles of quantum batteries. *Physical Review E*, 87(4), April 2013.

[4] A. E Allahverdyan, R Balian, and Th. M Nieuwenhuizen. Maximal work extraction from finite quantum systems. *Europhysics Letters (EPL)*, 67(4):565–571, August 2004.

[5] Felix C Binder, Sai Vinjanampathy, Kavan Modi, and John Goold. Quantacell: powerful charging of quantum batteries. *New Journal of Physics*, 17(7):075015, July 2015.

[6] Francesco Campaioli, Stefano Gherardini, James Q. Quach, Marco Polini, and Gian Marcello Andolina. Colloquium : Quantum batteries. *Reviews of Modern Physics*, 96(3), July 2024.

[7] Francesco Campaioli, Felix A. Pollock, Felix C. Binder, Lucas Céleri, John Goold, Sai Vinjanampathy, and Kavan Modi. Enhancing the charging power of quantum batteries. *Phys. Rev. Lett.*, 118:150601, Apr 2017.

[8] Francesco Caravelli, Ghislaine Coulter-De Wit, Luis Pedro García-Pintos, and Alioscia Hamma. Random quantum batteries. *Phys. Rev. Res.*, 2:023095, Apr 2020.

[9] Alberto Giuseppe Catalano, Salvatore Marco Giampaolo, Oliver Morsch, Vittorio Giovannetti, and Fabio Franchini. Frustrating quantum batteries, 2023.

[10] Debanjan Chowdhury, Antoine Georges, Olivier Parcollet, and Subir Sachdev. Sachdev-ye-kitaev models and beyond: Window into non-fermi liquids. *Reviews of Modern Physics*, 94(3), September 2022.

[11] Hrant Gharibyan, Masanori Hanada, Stephen H. Shenker, and Masaki Tezuka. Onset of random matrix behavior in scrambling systems. *Journal of High Energy Physics*, 2018(7), July 2018.

[12] Olivier Giraud, Nicolas Macé, Éric Vernier, and Fabien Alet. Probing symmetries of quantum many-body systems through gap ratio statistics. *Physical Review X*, 12(1), January 2022.

[13] Yingfei Gu, Alexei Kitaev, Subir Sachdev, and Grigory Tarnopolsky. Notes on the complex sachdev-ye-kitaev model. *Journal of High Energy Physics*, 2020(2), February 2020.

[14] Ju-Yeon Gyhm, Dario Rosa, and Dominik Šafránek. Minimal time required to charge a quantum system. *Physical Review A*, 109(2), February 2024.

[15] Duc Tuan Hoang, Friederike Metz, Andreas Thomasen, Tran Duong Anh-Tai, Thomas Busch, and Thomás Fogarty. Variational quantum algorithm for ergotropy estimation in quantum many-body batteries. *Physical Review Research*, 6(1), January 2024.

[16] Juan Maldacena, Stephen H. Shenker, and Douglas Stanford. A bound on chaos. *Journal of High Energy Physics*, 2016(8), August 2016.

[17] Juan Maldacena and Douglas Stanford. Remarks on the sachdev-ye-kitaev model. *Physical Review D*, 94(10), November 2016.

[18] L. Mandelstam and Ig. Tamm. *The Uncertainty Relation Between Energy and Time in Nonrelativistic Quantum Mechanics*, pages 115–123. Springer Berlin Heidelberg, Berlin, Heidelberg, 1991.

[19] Patrick Orman, Hrant Gharibyan, and John Preskill. Quantum chaos in the sparse syk model, 2024.

[20] Soshun Ozaki and Hosho Katsura. Disorder-free sachdev-ye-kitaev models: Integrability and a precursor of chaos, 2024.

[21] Dario Rosa, Davide Rossini, Gian Marcello Andolina, Marco Polini, and Matteo Carrega. Ultra-stable charging of fast-scrambling syk quantum batteries. *Journal of High Energy Physics*, 2020(11), November 2020.

[22] Davide Rossini, Gian Marcello Andolina, and Marco Polini. Many-body localized quantum batteries. *Phys. Rev. B*, 100:115142, Sep 2019.

[23] Davide Rossini, Gian Marcello Andolina, Dario Rosa, Matteo Carrega, and Marco Polini. Quantum advantage in the charging process of sachdev-ye-kitaev batteries. *Phys. Rev. Lett.*, 125:236402, Dec 2020.

[24] Julian Sonner and Manuel Vielma. Eigenstate thermalization in the sachdev-ye-kitaev model. *Journal of High Energy Physics*, 2017(11), November 2017.

[25] Shenglong Xu, Leonard Susskind, Yuan Su, and Brian Swingle. A sparse model of quantum holography, 2020.